Three-dimensional nonlinear dynamics of prestressed active filaments: Flapping, swirling, and flipping

Soheil Fatehiboroujeni*
Department of Mechanical Engineering, University of California, Merced, California 95343, USA

Arvind Gopinath†
Department of Bioengineering, University of California, Merced, California 95343, USA

Sachin Goyal
Department of Mechanical Engineering, University of California, Merced, California 95343, USA
and Health Sciences Research Institute, University of California, Merced, California 95343, USA

(Received 20 May 2020; revised 22 November 2020; accepted 24 December 2020; published 25 January 2021)

Initially straight slender elastic filaments or rods with constrained ends buckle and form stable two-dimensional shapes when prestressed by bringing the ends together. Beyond a critical value of this prestress, rods can also deform off plane and form twisted three-dimensional equilibrium shapes. Here, we analyze the three-dimensional instabilities and dynamics of such deformed filaments subject to nonconservative active follower forces and fluid drag. We find that softly constrained filaments that are clamped at one end and pinned at the other exhibit stable two-dimensional planar flapping oscillations when active forces are directed toward the clamped end. Reversing the directionality of the forces quenches the instability. For strongly constrained filaments with both ends clamped, computations reveal an instability arising from the twist-bend-activity coupling. Planar oscillations are destabilized by off-planar perturbations resulting in twisted three-dimensional swirling patterns interspersed with periodic flipping or reversal of the swirling direction. These striking swirl-flip transitions are characterized by two distinct timescales: the time period for a swirl (rotation) and the time between flipping events. We interpret these reversals as relaxation oscillation events driven by accumulation of torsional energy. Each cycle is initiated by a fast jump in torsional deformation with a subsequent slow decrease in net torsion until the next cycle. Our work reveals the rich tapestry of spatiotemporal patterns when weakly inertial strongly damped rods are deformed by nonconservative active forces. Taken together, our results suggest avenues by which prestress, elasticity, and activity may be used to design synthetic macroscale pumps or mixers.

DOI: 10.1103/PhysRevE.103.013005

I. INTRODUCTION

The deformation of slender rods and filaments has been the subject of enquiry since 1757 when Euler developed a framework to analyze and study the instability of axially loaded elastic columns and beams [1]. His seminal work provided estimates of critical loads that result in elastic instabilities now known as Euler buckling. These values were further refined using a higher order theory by Lagrange [2,3]. Paraphrasing Truesdell [4], the theoretical foundation of these studies and others that followed in their wake were grounded in two main ideas—the first by Hooke who proposed that the displacement of an elastic body was in proportion to the load causing the displacement, and the second by Bernoulli's hypothesis that the curvature in a bent rod was in proportion to the local resisting moment. General principles and concepts identified in the interrogation of Euler buckling have since played central roles in understanding the mechanics and dynamics of slender structures across disciplines including structural engineering [5–13], botany [14], and biophysics [15–22].

Over the last many decades, various linear and nonlinear theories have been proposed to analyze elastic instabilities for two modalities of external forces or loads. The first comprises conservative forces derivable from potentials such as self-loading due to gravity [23,24]. For these, stability can be deduced from extremizing energy functionals and taking into account any work done at boundaries. Mathematically, this implies that static stable shapes are derived by minimizing suitably derived Hamiltonians founded on self-adjoint formulations—an approach that has been utilized [23–25] and discussed extensively.

More recently, attention has turned to the study of elastic structures and systems under the action of active *nonconservative forces*. This class includes follower forces—forces that are always aligned along the centerline of the filament and move with it as it deforms. The engineering motivation for studying these came initially from problems in aeroelasticity [26] and flow-induced energy harvesting [27]. Recent focus has however been on problems involving follower forces in bio-inspired filamentous systems. Motivated by the manner in

*sfatehiboroujeni@ucmerced.edu
†agopinath@ucmerced.edu

 ©2021 American Physical Society

which eukaryotic cilia and flagella oscillate with distinct frequencies and wavelengths [28–35], significant work has gone into developing synthetic mimics that generate similar functionality such as locomotion, mixing, and mechanosensing [13,36–38]. Abstracting the key components of the immensely complicated biological systems, these analogs exploit fluid dissipation, and elasticity combined with magnetic, electric, or chemical fields to induce follower forces that yield buckling and motion [39–43]. Similarly, a recent experimental setup [44] presents how Coulomb friction may result in follower forces and induce deformation.

In contrast to filaments subject to conservative forces, the stability and dynamics of structures animated by follower forces cannot be examined by energy based arguments. This is due to the non-self-adjoint nature of the equations and boundary conditions [23–25,45–51]. Instead, time dependent evolution equations (dynamical equations) derived using variants of the Kirchhoff-Love theory are appropriate and have been used to analyze the onset of instabilities and nonlinear patterns in these systems [29,52–55]. As part of this effort, studies have also focused on elucidating material constitutive laws [56,57].

However, a significant fundamental gap in the literature exists. Most current theories relate to filaments or rods that are not prestressed (equivalently, not prestrained) and further are only partially constrained; that is, in most cases the base state is an uncompressed rod with a straight shape [29,52–55]. In realistic scenarios and contexts, however, rods and filaments that are subject to deforming forces and torques start off from shapes that are neither planar nor stress-free. Prestressed and twisted three-dimensional shapes abound in nature at all scales; examples include buckling growing tendrils [58,59], the curling of ropes hitting a surface [60], torsionally constrained DNA looping mediated by protein binding [61,62], self-contact driven DNA buckling [63,64], and relaxation of DNA supercoils by topoisomerases [65]. We note that a prestressed filament clamped at both ends—being both prestressed and strongly constrained at the boundaries—is expected to have different dynamics than stress-free cantilevers.

In this article, we attempt to bridge this gap in the current research. In previous work [66], we analyzed the planar purely two-dimensional instabilities of rods; base states and perturbations were thus restricted to only planar forms. In our earlier paper we analyzed the planar (two-dimensional) instability of rods with fixed-fixed boundary conditions, with only planar base states, and subject to only planar perturbations. In this work, we investigate the effect of follower forces on the stability of rods with both fixed-fixed and pinned-fixed boundary conditions, under fully three-dimensional conditions. That is, the base states can be planar or twisted and the perturbations similarly can be purely two-dimensional or fully three-dimensional. Using detailed computations built on the continuum nonlinear Kirchhoff-Love rod model [66], we explore and reveal two- and three-dimensional instabilities—flapping, swirling, and flipping—that arise when thin active elastic filaments are subject to a competition between dissipation and activity. The three-dimensional instability that we term the swirl-flip instability and that is the dominant focus of this paper has not been studied elsewhere, especially in the context of actively driven filament systems. To the best of our knowledge, a nonlinear and fully three-dimensional analysis as ours has also not been presented.

The organization of this article is as follows. In Sec. II, we present the continuum rod model for animated geometrically nonlinear slender elastic rods also subject to fluid drag. In Sec. III, we summarize results for filaments with planar prestressed base states, and then we move to results for base states that are fully three-dimensional. To isolate the effect of boundary conditions from the role of prestress and activity, we present here results for two practically important types of boundary constraints—clamped-clamped rods and pinned-clamped rods in the planar postbuckling regime. We then turn to rods with clamped-clamped constraints in the secondary bifurcation (bent and twisted) regime. We find that nonplanar base states if activated by any nonzero follower force give rise to a swirling (purely rotational) motion around the end-to-end axis of the rod. In addition, we find that swirling oscillations undergo a sudden reversal of direction, i.e., a periodic flipping akin to the phenomena of relaxation oscillations seen in diverse fields such as lasers, cellular phenomena, and electronic circuits [67]. We conclude in Secs. IV and V with a summary of results, their significance, and suggestions to extend current work and motivate future theoretical work.

II. COMPUTATIONAL SCHEME: MODEL FOR AN ACTIVE CONTINUUM ROD

A. Governing equations following the Kirchhoff approach

The continuum rod model that we use follows Kirchhoff's approach [68] assuming each cross section of the rod to be rigid and is described in detail elsewhere [69]. Here we provide a summary. Note that we use the description "slender rod" and "filament" interchangeably in what follows.

We start with a rod with length L when straight (undeformed) and diameter d. The rod is composed of a continuum elastic material; the mass density (mass per unit length) is m. Let s parametrize the arclength of the rod and thus the location of material points along its backbone (centerline), t denote the time, and tensor $\mathbf{I_m}(s)$ denote the moment of inertia per unit length. In the Kirchhoff-Love framework, the equilibrium equations [Eqs. (1) and (2)] and the compatibility conditions [Eqs. (3) and (4)] are

$$m\left(\frac{\partial \mathbf{v}}{\partial t}+\boldsymbol{\omega}\times\mathbf{v}\right)-\left(\frac{\partial \mathbf{f}}{\partial s}+\boldsymbol{\kappa}\times\mathbf{f}\right)-\mathbf{f_e}=\mathbf{0}, \tag{1}$$

$$\mathbf{I_m}\cdot\frac{\partial \boldsymbol{\omega}}{\partial t}+\boldsymbol{\omega}\times\mathbf{I_m}\cdot\boldsymbol{\omega}-\left(\frac{\partial \mathbf{q}}{\partial s}+\boldsymbol{\kappa}\times\mathbf{q}\right)+\mathbf{f}\times\mathbf{r}-\mathbf{q_e}=\mathbf{0}, \tag{2}$$

$$\frac{\partial \mathbf{r}}{\partial t}+\boldsymbol{\omega}\times\mathbf{r}-\left(\frac{\partial \mathbf{v}}{\partial s}+\boldsymbol{\kappa}\times\mathbf{v}\right)=\mathbf{0}, \tag{3}$$

$$\frac{\partial \boldsymbol{\kappa}}{\partial t}-\left(\frac{\partial \boldsymbol{\omega}}{\partial s}+\boldsymbol{\kappa}\times\boldsymbol{\omega}\right)=\mathbf{0}. \tag{4}$$

Equations (1)–(4) encapsulate both effects of geometry as well as the forcing driving the filament away from its straight base shape. Geometry dictates that the centerline tangent vector is $\mathbf{r}(s,t)$ and its variations along the length $(\partial\mathbf{r}/\partial s)$ capture shear and extension. In this paper, such variations are assumed

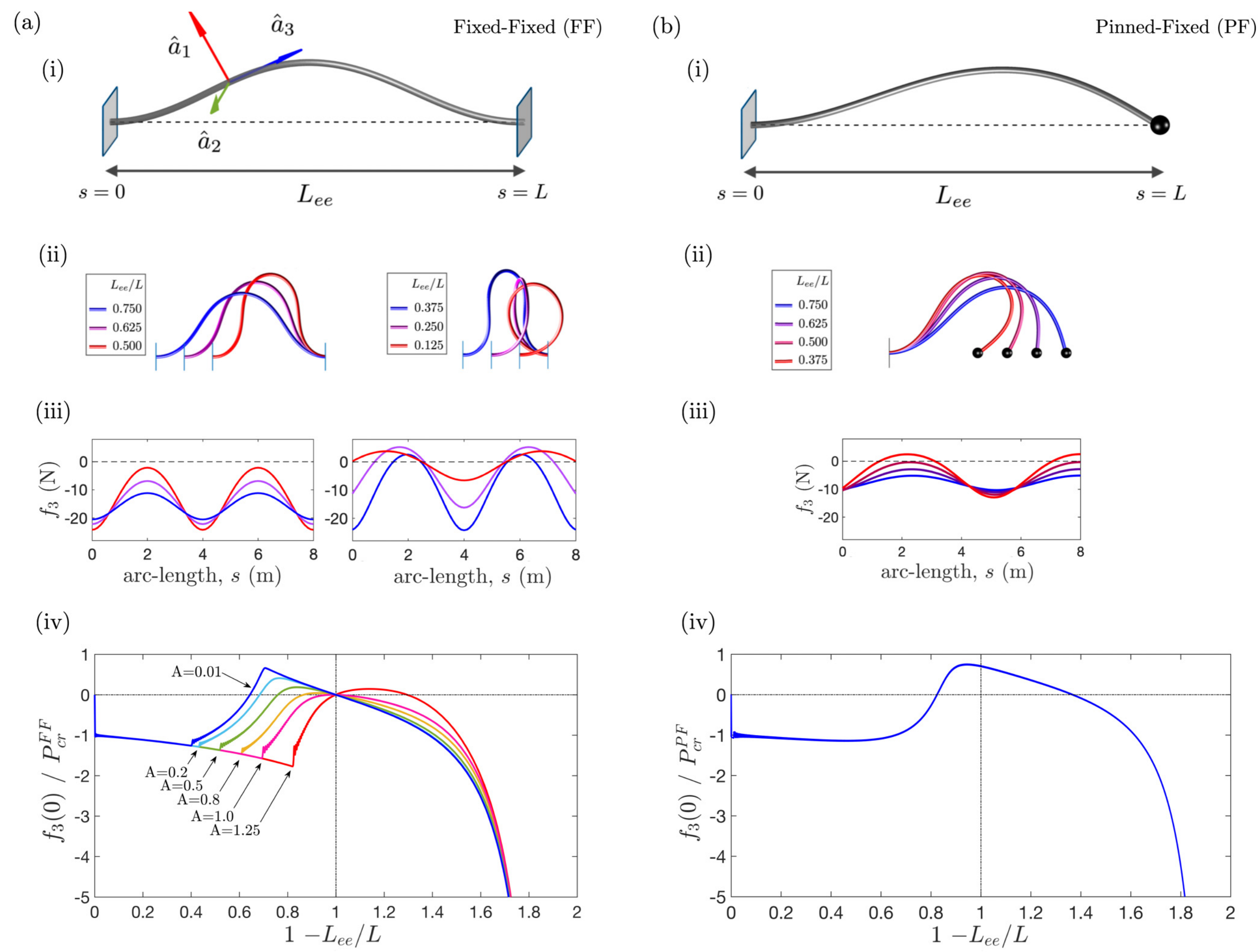

FIG. 1. Computational results relating to two- and three-dimensional buckling deformations of an inextensible, unshearable passive elastic slender rod (no follower forces). The rod has undeformed length L, uniform diameter $d \equiv \epsilon L$ with $\epsilon \ll 1$, and is comprised of linearly elastic material with Young's modulus E (Table I). The rod is then prestressed by pushing the ends together. The ratio of torsional to bending stiffnesses is A. Ensuing deformation fields are analyzed using the Kirchhoff-Love equations as in Sec. II. To specify the shape of the filament, we employ a reference coordinate system defined by unit vectors $\hat{\mathbf{a}}_1$, $\hat{\mathbf{a}}_2$, and $\hat{\mathbf{a}}_3$ as shown. Tile (a) summarizes results for a fixed-fixed (FF) boundary condition while tile (b) summarizes results for pinned-fixed (PF) boundary conditions. (a) (i) is a schematic representations of a prestressed, buckled fixed-fixed rod with end-to-end distance $L_{\rm ee} < L$ while (b) (i) is the corresponding sketch for the pinned-fixed rod. Arclength s parametrizes the location of Lagrangian material points in both. As illustrated in (a) (ii) and in (b) (ii), the initially straight filament buckled to a stable, static planar shape when load on the boundary, $f_3(0)$, the component along $\hat{\mathbf{a}}_3$, reaches the Euler buckling value. This compression or prestress is controlled by the value of the slack $1 - L_{\rm ee}/L$. The critical values are $P_{\rm cr}^{\rm FF} = 4\pi B/L^2$ for fixed-fixed and $P_{\rm cr}^{\rm PF} = 2.045\pi B/L^2$ for pinned-fixed conditions. Fixing $A = 0.8$, we determined the evolution of static shapes as well as distribution of internal forces in the tangential direction, f_3, as a function of $L_{\rm ee}/L$ for both FF and PF cases. These are shown in rows (a) and (b) (ii) and (a) and (b) (iii), respectively. The corresponding bifurcation diagram indicating the variation in $f_3(0)$ as a function of $L_{\rm ee}/L$ is shown in (a) (iv) and (b) (iv). For the specific case of the FF filament, we find that beyond a critical value of compression (equivalently $1 - L_{\rm ee}/L$), planar buckling shapes are not absolutely stable; the configurations stable to both in-plane and out-of-plane disturbances are three-dimensional twisted shapes emerge. The onset of this secondary bifurcation governed by the torsional-to-bending stiffness ratio, A, shown in (a) (iv). The two-dimensional shapes prior to the secondary bifurcation as well as twisted shapes after secondary bifurcation are shown in (a) (ii) for the specific instance $A = 0.8$. The small oscillations in (a) (iv) are numerical simulation artifacts partly due to very weakly non-quasistatic nature of the manner in which the rod (filament) is loaded.

to be zero to ensure inextensibility and unshearability; therefore $\mathbf{r}$ becomes constant and collinear with the cross-sectional normal vector $\hat{\mathbf{a}}_3$ [see Fig. 1(a) (i)]. Vectors $\mathbf{f_e}$ and $\mathbf{q_e}$ are the external distributed force and moment, respectively. The spatial and the temporal derivatives in Eqs. (1)–(4) are relative to the body-fixed frame $(\hat{\mathbf{a}}_1, \hat{\mathbf{a}}_2, \hat{\mathbf{a}}_3)$.

B. Constitutive laws relating bending to curvature

The unknown variables in Eqs. (1)–(4) are the vector $\boldsymbol{\kappa}(s,t)$ that captures two-axis bending and torsion, the vectors $\mathbf{v}(s,t)$ and $\boldsymbol{\omega}(s,t)$ that represent the translational and the angular velocities of each cross section, respectively, and the vector $\mathbf{f}(s,t)$ that represents internal shear force and tension. For

TABLE I. Representative numerical values for the properties of the rod, and for the drag coefficients used in the simulations. The density of the surrounding fluid is taken to be the density of water and kept constant. The mass per unit length of the slender rod is assumed to be constant as well for all our computations. Material properties G and E are related through the Poisson ratio ν via $G = E/2(1+\nu)$. Additional computations with varying ratios $A \equiv B/T$ were further conducted using different values of G/E obtained by varying Poisson ratio.

Quantity	Symbol	Value
Bending stiffness	B	29.2×10^{0} N m^2
Torsional stiffness	T	23.3×10^{0} N m^2
Mass per unit length	m	2.0×10^{-1} kg/m
Length	L	8.0×10^{0} m
Diameter	d	9.6×10^{-3} m
Normal drag coefficient	$C_{\perp}$	1.0×10^{-1}
Tangential drag coefficient	$C_{\parallel}$	1.0×10^{-2}
Surrounding fluid density	ρ_{f}	1.0×10^{3} kg/m^3
Surrounding fluid viscosity	μ	2.5×10^{-3} Pa s

simplicity, we relate the internal moment vector $\mathbf{q}(s,t)$ in the angular momentum equation (2) to $\boldsymbol{\kappa}(s,t)$ through the linear constitutive law

$$\mathbf{q}(s,t) = \mathbf{B} \cdot \boldsymbol{\kappa}, \tag{5}$$

where $\mathbf{B}(s)$ represents the rod's bending and torsional stiffness.

Without the loss of generality, we choose the body-fixed frame to coincide with the principal torsion-flexure axes of the rod, so that the stiffness tensor $\mathbf{B}$ for an isotropic rod can be expressed as a diagonal matrix

$$[\mathbf{B}] = \begin{bmatrix} B & 0 & 0 \\ 0 & B & 0 \\ 0 & 0 & T \end{bmatrix}. \tag{6}$$

In Eq. (6), E is the Young's modulus, G is the shear modulus, and B and T are the bending and torsional stiffness, respectively. The ratio of the two moduli

$$A \equiv \frac{T}{B}$$

serves as an independent parameter that we choose to vary in our computations along with the magnitude of the active force, F.

In our simulations, we kept filament geometry and material properties constant. For a slender filament or rod with circular cross section and uniform properties, the second moment of area I and the polar moment of inertia J are proportional. Furthermore, G and E are related through the Poisson's ratio ν via $G = E/2(1+\nu)$ for a linearly elastic and isotropic material. In addition to computations using parameters listed in Table I, further calculations were conducted by varying the Poisson's ratio. For constant filament geometry (radius and length), this amounts to changing A while keeping I and J fixed.

We are interested in general features of oscillations under follower forces that are translatable to macroscale systems; therefore we have chosen parameter values corresponding to a macroscopic rod. Nonetheless, to understand how physical properties of the rod govern its mechanical response regardless of the range of values chosen here, we work with nondimensional parameters such as slenderness ratio, L/d, torsion-to-bending ratio, A, and nondimensional force, $FL^3/(4\pi^2 B)$.

C. External forces: Active forces

In addition to internal forces and torques that act on each elemental section of the filament, we have externally exerted forces and torques on the system. These terms could be a consequence of boundary conditions imposed at the ends at $s = 0$ and at $s = L$. Additionally, in the interior domain of the filament $0 < s < L$, external forces acting on segments of the rod can arise from two independent physical processes or actions. The first one is the active animating force treated here as a distributed follower force that enters in (1) as the force density (per unit length) $F\boldsymbol{t}$. This force always acts along the local instantaneous tangent vector, $\boldsymbol{t}$, and is always directed (arclength-wise) toward the boundary at $s = 0$. For a straight rod this constitutes a compressive force that initiates the buckling process. The active force thus pumps energy into the system.

D. External forces: Fluid drag

The second type of external force we consider is dissipative fluid drag, $\mathbf{f_M}$, and serves to draw and extract energy away from the system. As a result, total external force is calculated by $\mathbf{f_e} = F\boldsymbol{t} + \mathbf{f_M}$. Note that in general, the resultant fluid drag comprises both inertia forces in phase with the local flow acceleration (the functional form as found in potential flow theory) and drag components dependent on the relative far-field velocity (of the form for a rigid body placed in a steady flow). The drag component furthermore can be quadratic (nonlinear) or linear depending on the Reynolds number characterizing the flow patterns. Here, we use tractable forms for the drag coefficients and analyze results in two complementary limits. We use the Morison drag form for the nonlinear high Reynolds number inertially dominated limit, and Stokes drag for the low Reynolds number viscously dominated limit.

Note that *a priori* we cannot know the dynamics of the rod as it deforms and thus timescales and length scales associated with the deformation as these are emergent properties. Since our focus is on the activity-elasticity coupling with fluid drag playing a purely dissipative role, it is reasonable to seek a low-dimensional form for the fluid drag that encapsulates the essential physics while still allowing for a tractable problem. Thus we look for effective drag coefficients that depend on fluid properties and the speed at which the deforming filament or rod moves through the ambient fluid ignoring edge effects and coarse-graining details of the fluid flow (Appendix A). Our aim is not to solve the fully coupled nonlinear time-dependent solid-fluid problem but to use a reduced description of the fluid drag on the filament that allows for exploration of the role activity plays in enabling and sustaining oscillations.

1. *Quadratic Morison drag*

We look at the nature and form of the fluid drag valid typically at high swirling speeds (high Reynolds numbers) where the fluid drag has a complex form (Appendix A). The Morison formula captures the hydrodynamic resistive forces applied to cylindrical structures in oscillatory or steady flows [70–72] reasonably well. The local drag force calculated by the Morison equation as in (7) depends on Reynolds number and surface roughness. To calculate the drag force $\mathbf{f}_{\mathrm{M}}$, we here choose to implement the equation in the form used in previous work [66,70],

$$\frac{-\mathbf{f}_{\mathrm{M}}}{\frac{1}{2}\rho_{\mathrm{f}}d} = C_{\perp}|\mathbf{v}\times\mathbf{t}|\mathbf{t}\times(\mathbf{v}\times\mathbf{t}) + \pi C_{\parallel}(\mathbf{v}\cdot\mathbf{t})|\mathbf{v}\cdot\mathbf{t}|\mathbf{t}, \qquad (7)$$

where ρ_{f} is the fluid density, d is diameter of the rod, $\mathbf{t}$ is the unit tangent vector to centerline, and $C_{\perp}$ and $C_{\parallel}$ are the normal and tangential components of drag coefficients, respectively. These are chosen to be constants (please see discussion in Appendix A that justifies this lower-dimensional form for the purposes our our analysis).

2. Linear Stokes drag

In the limit of very low speeds characterizing the rod deformation such as low swirling rates and/or bending oscillation frequencies, the fluid resistance is primarily due to viscous drag and without inertial components. In this limit, the drag force per unit length of the rod (even as it is deforming and moving) can be approximated using the resistive force theory (see Refs. [52–55]). To leading order, the drag per unit length may be written as a linear functional of the velocity of the rod relative to the far-field ambient (no flow) value and takes the form

$$-\mathbf{f}_{\mathrm{S}} = C_n\mathbf{t}\times(\mathbf{v}\times\mathbf{t}) + C_t(\mathbf{v}\cdot\mathbf{t})\mathbf{t}. \qquad (8)$$

In this equation

$$C_n \approx \frac{4\pi\mu}{\ln(L/d)}, \quad \frac{C_t}{C_n} \approx 2.$$

In the Stokes limit, density does not come into the drag expression and it is instead the fluid viscosity μ that is important.

In our simulations in order to keep the simulation time reasonable while still being able to capture relevant dynamics, we set the viscosity of the surrounding fluid to be slightly higher than the viscosity of the water. This is reasonable also because the relevant situations such as in microfluidics where our results may be applied usually involve liquids that are polymeric with viscosities greater than that of water.

III. RESULTS: COMPUTATIONAL SIMULATIONS AND DISCUSSION

In previous work [66], we investigated the effect of both linear (Stokes) and quadratic (Morison) drag on planar flapping of clamped rods. While the form of the drag force has a quantitative effect on the amplitude and frequency of *two-dimensional* flapping oscillations, we found that once oscillations were initiated, the qualitative response was similar.

In the following sections and discussions, we focus on Morison drag, that is, the quadratic form of the drag. Therefore, unless explicitly stated, our results are to be taken as corresponding to this form of the fluid force. At the same time we present results to confirm that changing the drag to the linear Stokes form does not qualitatively change the spatiotemporal patterns we observe. Specifically, transitions to stable three-dimensional swirling and the swirl-flip transitions we identify are independent of the precise form of the drag.

A. Solution methodology, accuracy, and convergence

To compute the numerical solution of this system, subjected to necessary and sufficient initial and boundary conditions, the *generalized-α* method is adopted. It is a second order, implicit, and unconditionally stable method with controllable numerical dissipation. Discretization parameters used in space and time are respectively $ds = 0.1$ m and $dt = 0.01$ s. We varied the value of dt and tested for convergence. A detailed description of this numerical scheme applied to the rod formulation is given in [69] and references therein. Our computational model has been validated by comparing the critical value of the follower force in the planar cantilever scenario with analytical results of Beck's column [66]. In this paper, we analyze the spatiotemporal response and long-time stable dynamical states attained by prestressed rods with fixed-fixed (FF) and pinned-fixed (PF) boundary conditions subject to and animated by a uniformly distributed follower force.

In all the computations, an initially straight cylindrical rod is used with the properties given in Table I, chosen to represent a soft filament. These parameters helped us run our simulations in a reasonable time while still being able to capture the complete range of dynamical response. Before applying the distributed follower force, the prestress is generated by axial compression of the rod that leads to buckled equilibrium shapes as shown in Fig. 1. Starting from a relaxed and straight cylindrical rod, we load the filaments quasistatically to always remain close to the equilibrium configuration. Once the desirable level of prestress is achieved (defined in terms of the end-to-end distance, L_{ee}) we allow the small vibrations generated during the quasistatic loading to decay before the application of follower forces. The buckled shapes can be planar or out-of-plane and are described next, before exploring the effects of follower force.

B. Buckled shapes in the absence of follower force

Figures 1(a) and 1(b) show the postbuckling equilibria for FF and PF boundary conditions, respectively. For both the boundary conditions, the buckling onsets in plane as the compressive load $f_3(0)$ reaches Euler buckling load, which is $P_{\mathrm{cr}} = 4\pi B/L^2$ for FF and $P_{\mathrm{cr}} = 2.045\pi B/L^2$ for PF conditions. The compressive load $f_3(0)$ initially increases with the prestress $1 - L_{\mathrm{ee}}/L$ in each case. ESM Movie 1 in the Supplemental Material [73] shows the quasistatic simulation of how the rod shapes evolve for $A = 0.8$.

For the FF case, however, which is torsionally constrained, once compression increases beyond a critical limit (for example, $1 - L_{\mathrm{ee}}/L \approx 0.60$ for $A = 0.8$), planar buckled shapes become unstable and the rod transitions to energetically more favorable out-of-plane configurations that allow for the partial storage of strain energy in torsion [70,74]. This critical limit of secondary bifurcation increases as the torsional-to-bending stiffness ratio, $A = T/B$ increases, as depicted in the bifurcation diagram of Fig. 1(a) (iv). Figure 1(a) (ii) for instance shows both the stable two-dimensional shapes (for prestress less than that required for secondary bifurcation) as well as the fully twisted, three-dimensional stable shapes attained after secondary bifurcation. Previous studies by one of us have revealed (see also Appendix A, Fig. 10) that the out-of-plane buckled shapes have smaller bending energy and larger torsional energy in such a way that a net energetic advantage is reached for out-of-plane configurations, as soon as the end-to-end compression goes beyond a critical limit.

In the PF case, by contrast, which is not torsionally constrained, no secondary bifurcation emerges by increasing the end-to-end compression. ESM Movie 2 in the Supplemental Material [73] demonstrates quasistatic simulation used to generate the results for the equilibria shown in Fig. 1(b). Note that Fig. 1(b) (iv) shows the bifurcation diagram for the PF case with Fig. 1(b) (ii) pictorially depicting the two-dimensional shapes that are determined via computation.

In the following sections we take a representative variety of stable buckled configurations as *base states* for exploring the dynamics under distributed follower forces with homogeneous intensity. In particular, we first focus on the range of end-to-end values with planar base states in both FF and PF scenarios for $A = 0.8$, i.e., the interval between points 1 and 2 in Fig. 1, bottom row ($0.1 \leqslant 1 - L_{ee}/L \leqslant 0.5$). Next, we focus on the out-of-plane buckled configurations of the FF scenario as base states. We also investigate the effect of A as well as overall material stiffness. The role of A is crucial as seen in the difference in the extent to which the three-dimensional base states curve and bend out of plane—illustrated in Fig. 2.

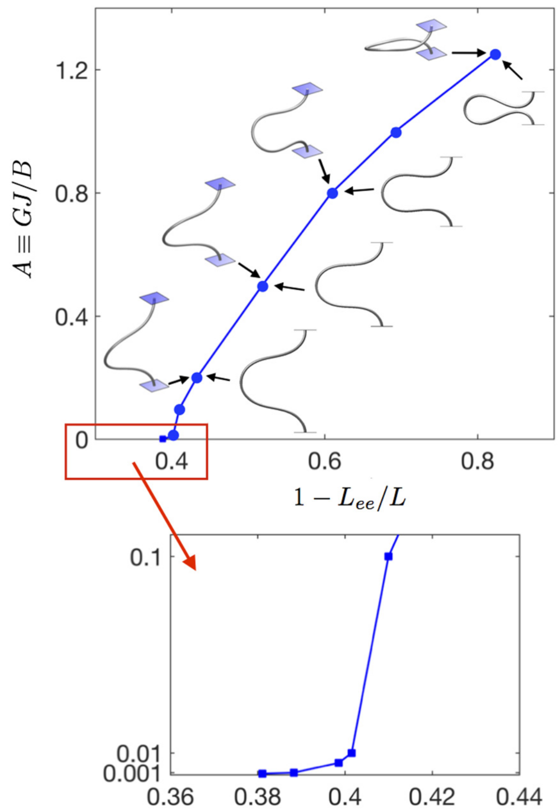

FIG. 2. For a slender rod with fixed-fixed (FF) boundary conditions, the ratio of torsional stiffness to bending stiffness, A, determines the slack $1 - L_{ee}/L$ at the onset of secondary bifurcation. This in turn sets the value of the internal compressional stress field at bifurcation. The shapes of the rod before (shapes on the right) and after (shapes on the left) the secondary bifurcation are shown for multiple A values. The inset in red rectangle indicates the sensitivity of the bifurcation to A. For very small values of A and as it approaches zero the slack threshold of the secondary bifurcation asymptotically decreases. The inset in red indicates the sensitivity of the bifurcation to A.

C. Flapping motion of planar base states

We next examine how the level of prestress (through the imposed value of L_{ee}/L) and the magnitude of the active force density F control (1) the stability of base states, and (2) the frequency of emergent oscillations. In order to generate the appropriate boundary conditions, we envision the rod or filament as being constrained at the ends via two clamps (for the FF case) or with a pin joint and a clamp (for the PF case). By controlling the end-to-end distance L_{ee}, we can then first generate stable buckled shapes, and then subsequently apply a follower force of intensity F along the local tangential direction of the rod's centerline.

Keeping the torsional-to-bending stiffness ratio constant at $A = 0.8$, for nearly the entire range of end-to-end values within the planar buckling regime, i.e., $0.05 \leqslant 1 - L_{ee}/L \leqslant 0.5$, our numerical analysis shows that beyond a critical value of the follower force, F_{cr}, buckled shapes no longer maintain static equilibrium, and planar oscillations—flapping oscillations—emerge when the rod is subject to any infinitesimal *planar* perturbations. This result is consistent with the onset of Hopf bifurcation that is obtained by linear stability analysis in the cantilever scenario [52–54,66]. ESM Movie 3 in the Supplemental Material [73] demonstrates an example of flapping oscillations with the spatiotemporal distribution of curvature and angular velocity in the fixed-fixed scenario. Fast Fourier transforms (using Matlab) of the midspan planar curvature field are used to compute the frequency of oscillations. In evaluating this, we choose a minimum of eight flapping cycles and typically more with these cycles sampled after initial transients have decayed and oscillations are stable.

Our analysis reveals that in both fixed-fixed and pinned-fixed scenarios, (1) F_{cr} increases linearly with prestress [see Fig. 3(a)], (2) near the critical point, the frequency of steady oscillations is sensitive to end-to-end distance [Fig. 3(b)], (3) and far from the critical point (for large values of F) the frequency of oscillations becomes independent of the prestress and scales roughly as $f_{\text{flap}} \sim F^{\frac{5}{6}}$. To rationalize the origin of the power law exponent, we consider period averaged quantities. For stable oscillations, the rate at which energy input into the system due to the action of the nonconservative follower forces balances the rate at which energy is dissipated by the fluid drag. For $F \gg F_{cr}$ the effects of slack (end-to-end distance L_{ee}) become negligible. The characteristic length over which significant deformations are accommodated is seen to be (see [54,66]) $\lambda \sim (B/|F|)^{\frac{1}{3}}$. The active energy is generated from the work done by follower forces (characteristic timescale here chosen as a period) is $\sim |F|\lambda^2\omega$ and thus the

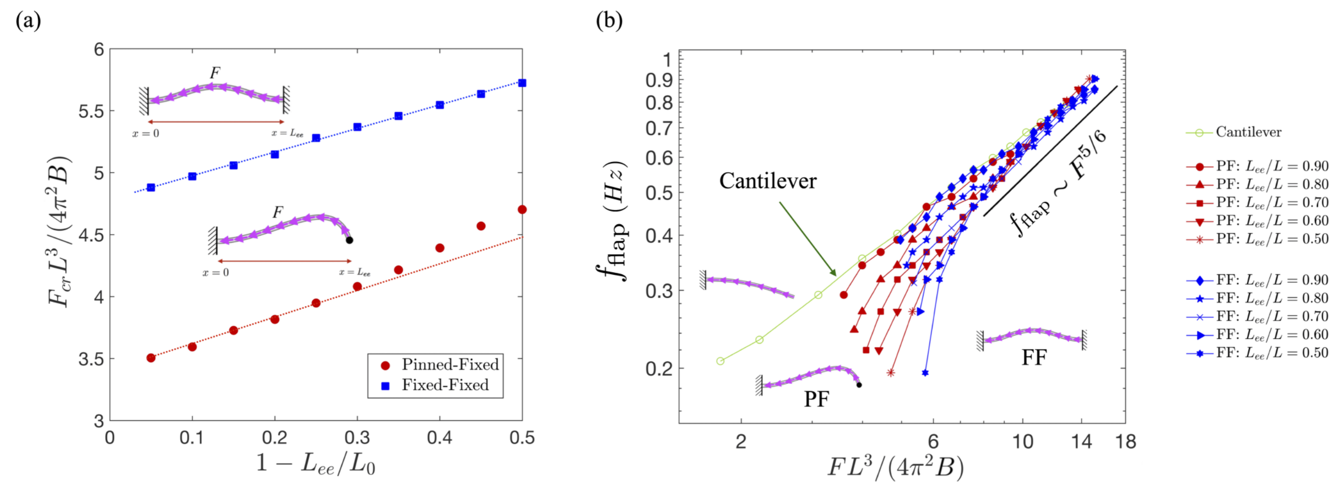

FIG. 3. Critical load for the onset of flapping, $F_{\rm cr}$, versus the compression rate, $1-L_{\rm ee}/L$, for both pinned-fixed (PF) and fixed-fixed (FF) scenarios varies with a linear relationship as shown in panel (a). Here, the pink arrows schematically represent the follower forces and indicate the direction in which these are exerted. Frequency of the flapping oscillations is plotted in panel (b) as a function of the force density, F, in logarithmic scales to illustrate two salient features: (1) as the follower force increases to values much larger than the critical limit, the effect of the prestress diminishes—far from criticality, similar frequencies are observed for all boundary conditions including the cantilever scenario—and (2) flapping frequencies in the limit $F \gg F_{\rm cr}$ scale roughly as $f_{\rm flap} \sim F^{\frac{5}{6}}$ consistent with theoretical prediction [66]. The pinned-fixed results may be compared to results for the fixed-fixed case which were analyzed previously by us. Note that significant deviations from linearity in (a) for the red data points correspond to the pinned-fixed case. For the particular case where the follower forces are directed always toward a clamped (fixed) end, $f_{\rm flap} \sim F^{5/6}$ when $F/F_{\rm cr} \gg 1$ independently of the pinned boundary.

energy dissipated by the drag force is $\sim C_{\rm eff}\lambda^4\omega^3$; here $C_{\rm eff}$ captures the effective drag as predicted from the Morison formula. A balance thus provides the relationship $\omega^3 \sim |F|^{\frac{5}{2}}/B$ consistent with our computations.

We further observe from Fig. 3(b) that for very large values of F, the nature of the boundary conditions seems to play a diminishing role in setting the value of the flapping frequency. This may be rationalized as follows. Far from the critical point, such as when the scaled follower force becomes one order of magnitude larger than the critical bifurcation force $[FL^3/(4\pi^2B) \approx 10]$, the effect of the prestress becomes dominated by (negligible with respect to) the relatively large forces induced by the active force, F.

Interestingly, we find that for the pinned-fixed scenario, the existence of oscillations depends on the direction of the follower forces. Specifically, when the follower force is directed from the clamped end toward the pinned end, no dynamical instability is induced [75]. This results suggests that altering boundary conditions independently of the strength of the follower forces or mechanisms generating these can be used to initiate or quench flapping oscillations.

Finally, we would like to point out that we do not investigate the onset of oscillations. In the system described by Eqs. (1)–(6), fluid drag, active forces, rod elasticity, and the inertia of the rod all enter into the picture. In earlier work on cantilever rods [66], we used a simple model to study how each of these influences the onset of oscillations and the location of the critical point. For the prestressed rods with inertia considered here, the critical points are not easily identifiable using time stepper techniques such as our model. Hence we focus on the fully nonlinear and large amplitude solutions far from the onset of oscillations.

D. Swirling motion with periodic reversal of nonplanar base states

For the range of parameters with nonplanar base shapes tested here ($0.60 \leqslant 1-L_{\rm ee}/L \leqslant 0.675$ and $A=0.8$ and $A=1.0$) we find purely rotational oscillations about the end-to-end axis to arise when a nonzero follower force is applied to the rod. We call this *swirling* motion. Figure 4 shows an example of the rod's configuration subject to an active distributed follower force in this range. By keeping the force constant and letting the dynamics reach a steady state we find that swirling rates decrease gradually until an abrupt reversal of direction, or *flipping* occurs (see Fig. 4 and, in the Supplemental Material [73], ESM Movie 4). Therefore, from simulations we extract a second characteristic timescale: the rate at which flips are observed.

The follower forces contribute moments that drive swirling and flipping. To understand these moments, refer to Fig. 4. Figure 4(a) demonstrates the shape of the rod in three orthogonal views and an isometric view with the distributed follower force. For swirling, we track the net moments of the follower force about the end-to-end axis, $\hat{\mathbf{e}}_3$. We first calculate the moment about an inertial frame of reference located at the middle of the two clamped ends. The net moment of the follower force $\mathbf{M_1} = (M_1, M_2, M_3)$ is calculated by the formula $\int_0^L(\mathbf{R_{c1}} \times F\mathbf{t})ds$ where $\mathbf{R_{c1}}$ is the position vector of the cross section at s with respect to the inertial frame $\{\hat{\mathbf{e}}_i\}$ located at the midpoint between the two clamps. The component of the moment generated about the end-to-end axis, $\mathbf{M_1}\cdot\hat{\mathbf{e}}_3$, is shown with blue color in panel (b) of Fig. 4, and is the main driver of the rotational swirling.

For flipping, we look at the moment about the Frenet-Serret normal vector at the midspan of the rod. This moment will

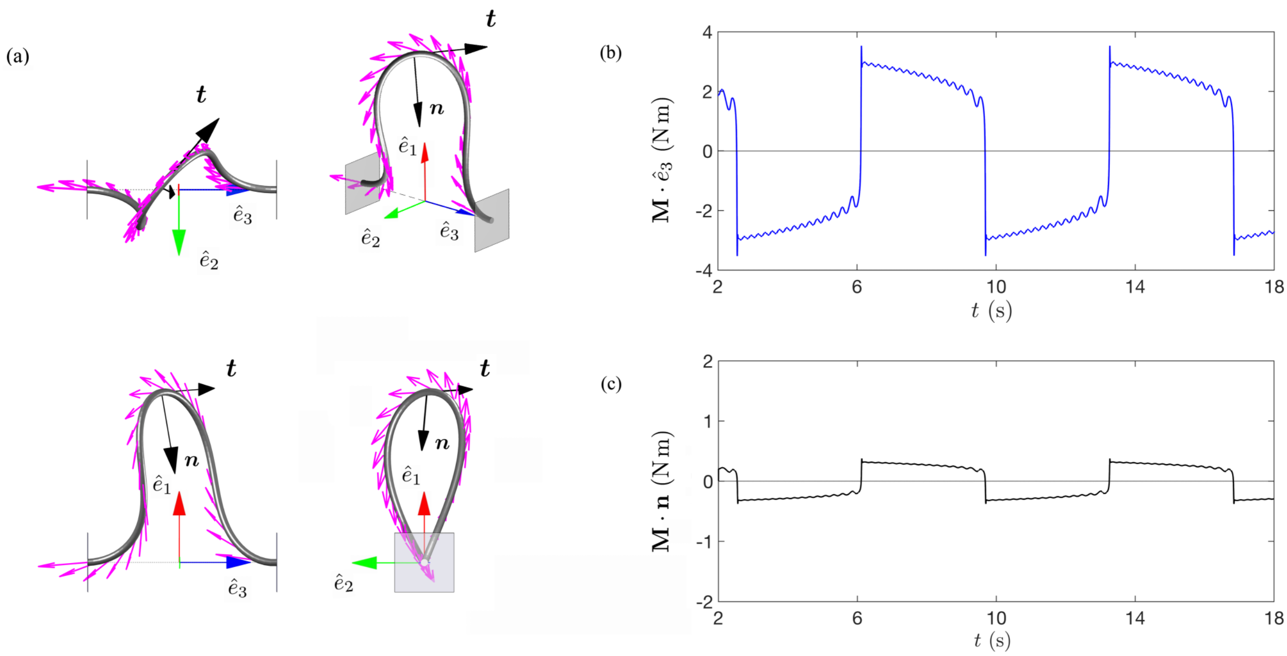

FIG. 4. Three orthogonal views and a perspective view of the rod with $1 - L_{ee}/L = 0.6$ and $A = 0.8$ after the application of a follower force with intensity $F = 4$ N/m are shown in panel (a) in *3rd angle projection* of engineering convention. The red, green, and blue arrows represent the global reference frame in each view. The distributed follower force, $F\mathbf{t}$, acts along the tangent vector and is shown here by magenta colored arrows, and gives rise to the swirling oscillations about the end-to-end axis, $\hat{e}_3$. The direction of swirling motion periodically flips along this axis. The net moment of the follower force $\mathbf{M_1} = (M_1, M_2, M_3)$ is calculated by the formula $\int_0^L(\mathbf{R_{c1}} \times F\mathbf{t})ds$ where $\mathbf{R_{c1}}$ in panel (b) is the position vector of the cross section at s with respect to the inertial frame $\{\hat{\mathbf{e}}_i\}$ located at the midpoint between the two clamps. The component of the moment generated about the end-to-end axis, M_3, is shown with blue curve in panel (b), and is the main driver of the rotational swirling. On the other hand, the effect of the moments generated about $\hat{e}_1$ and $\hat{e}_2$, i.e., M_1 and M_2, is to reduce the torsional deflection toward zero and to increase the bending deflection. This is ascertained by calculating the net moment of the follower force about the Frenet-Serret normal vector at the midspan of the rod, $\boldsymbol{n}(L/2)$. This moment is obtained using a similar formula $\mathbf{M_2} = \int_0^L(\mathbf{R_{c2}} \times F\mathbf{t})ds$ but $\mathbf{R_{c2}}$ is here defined as the position vector of the cross section at s with respect to the $s = L/2$ and is shown in panel (c). The Frenet-Serret normal vector $\boldsymbol{n}(L/2)$ lies in the plane of bending of the centerline and with the knowledge of the net moment along this axis we can determine the direction of the movement of the plane of bending. We find that the net moment about $\boldsymbol{n}(L/2)$ always drives the rod back into a planar configuration. In this process twist is reduced and bending is increased and it continues until the shape of the rod becomes nearly planar. Subsequent to this, a flip occurs and the swirling direction reverses.

also help explain why the twist is reduced and the bending is increased during the swirling motion before the flip happens. We calculate the Frenet-Serret normal vector of the rod centerline at the midspan, $\boldsymbol{n}(L/2)$, using the following equation which is valid for all values of s between zero and L:

$$\boldsymbol{n}(s) = \frac{1}{\sqrt{\kappa_1(s)^2 + \kappa_2(s)^2}}\boldsymbol{\kappa}(s) \times \boldsymbol{t}(s). \tag{9}$$

In this equation $\boldsymbol{\kappa}(s)$ is the curvature and twist vector, $\boldsymbol{t}(s)$ is the unit tangent vector to the centerline of the rod, and $\sqrt{\kappa_1(s)^2 + \kappa_2(s)^2}$ represents the principal curvature of the rod. Because the normal vector, $\boldsymbol{n}$, is in the plane of the curvature of the rod [pointing toward the center of curvature with the radius $1/\sqrt{\kappa_1(s)^2 + \kappa_2(s)^2}$], the net moment of the follower force about $\boldsymbol{n}(L/2)$ determines whether the plane of curvature rotates toward or away from the planar configuration. To calculate the net moment of the follower force about $\boldsymbol{n}(L/2)$ we use a similar integration, $\mathbf{M_2} = \int_0^L(\mathbf{R_{c2}} \times F\mathbf{t})ds$, where $\mathbf{R_{c2}}$ is defined as the position vector of the cross sections at s with respect to the $s = L/2$. Panel (c) of Fig. 4 demonstrates the component of this moment about $\boldsymbol{n}(L/2)$, namely $\mathbf{M_2} \cdot \boldsymbol{n}$. This moment drives the out-of-plane loop (or configuration) of the rod back toward a planar shape and ultimately flips it on the other side.

Note that prior to exertion of this force the base state has a plane of symmetry that passes through $\hat{e}_1$. Application of the follower force breaks this symmetry by deforming the rod as is obvious in Fig. 4(a). If the follower force were superimposed on the symmetric base state to calculate the flipping moment $\mathbf{M} \cdot \boldsymbol{n}$, it would be zero. It is the asymmetry in the shape caused by the follower force that contributes to a nonzero moment about $\boldsymbol{n}(L/2)$ and thus drives the flipping phenomenon. By contrast, the swirling moment would be nonzero even if it were calculated by superimposing the follower force on the symmetric base state.

Recognize that as the out-of-plane loop returns to planar shape, the twist must vanish, and the bending energy must increase. This is the reversal of out-of-plane bifurcation explained in [70], wherein the bending energy decreases with some increase in torsional energy reducing overall strain energy to favor the out-of-plane bifurcation. A detailed budget of energy exchange during oscillations is explained in the next subsection.

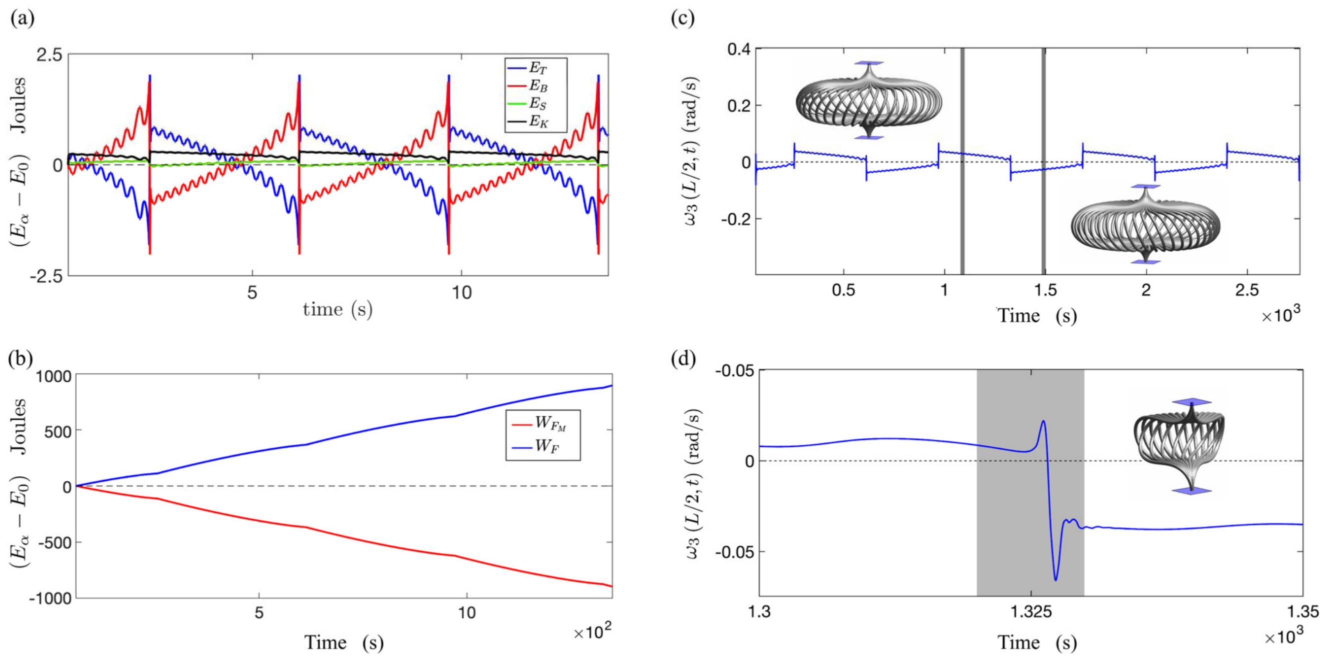

FIG. 5. Variations in time of torsional energy, E_T, bending energy, E_B, total strain energy, E_S, and kinetic energy, E_K, with respect to the energy levels at the base state, E_0, are shown in panel (a) and variations of energy dissipated by fluid drag, $W_{\mathbf{f}_M}$, and work done by follower force, W_F, are depicted in panel (b). The results reveal that a relatively small change occurs in both the strain energy (the green curve) and the kinetic energy (the black curve), while the torsional energy (blue curve) falls bellow its corresponding magnitude at the base state (E_0) and the bending energy increases to significantly larger values compared to the based state. As a measure of the swirling frequency, the component of the angular velocity about $\hat{a}_3$ at the midspan length is plotted in time for $|F| = 1$ N/m, $1 - L_{ee}/L = 0.60$, and $A = 0.8$ in panel (c). A set of superimposed shapes during an entire swirling cycle (the shaded interval) is also given in panels (c) and (d). Evolution of angular velocity at the midspan length during the flipping along with the rendition of the shapes is illustrated in panel (d).

E. Energy exchange during oscillations

In each flipping cycle which approximately takes about two orders of magnitude longer than a swirling cycle, the total strain energy slightly increases (less than 0.1% per cycle); the bending energy however increases significantly (about 4% per cycle) and the torsional energy decreases most significantly (about 100% per cycle). Expressions used to evaluate the torsional energy, E_T, bending energy, E_B, total strain energy, E_S, kinetic energy, E_K, energy dissipated by fluid drag, $W_{\mathbf{f}_M}$, and work done by follower force, W_F, from simulation results are given below, respectively,

$$E_s = \frac{1}{2}\int_0^L (\mathbf{B}\cdot\boldsymbol{\kappa})\cdot\boldsymbol{\kappa}\,ds = E_B + E_T$$
$$= \frac{1}{2}\int_0^L B(\kappa_1^2+\kappa_2^2)\,ds + \frac{1}{2}\int_0^L T\kappa_3^2\,ds, \tag{10}$$
$$E_K = \frac{1}{2}\int_0^L m(\mathbf{v}\cdot\mathbf{v})\,ds, \tag{11}$$
$$W_{\mathbf{f}_M} = \int_0^t\int_0^L (\mathbf{f}_M\cdot\mathbf{v})\,ds\,d\tau, \tag{12}$$
$$W_F = \int_0^t\int_0^L (F\mathbf{t}\cdot\mathbf{v})\,ds\,d\tau. \tag{13}$$

Figure 5(a) demonstrates various forms of energy relative to the energy levels of the base state configuration after a unit follower force is applied to a buckled rod with $1 - L_{ee}/L = 0.60$ and $A = 0.8$. Once the force is applied and rotational (swirling) cycles begin, we observe a gradual decrease in kinetic energy and a gradual increase in total strain energy; see Figs. 5(a) and 5(c). With further swirling, when enough of torsional energy is converted to bending, the rod reaches a nearly planar configuration that is not stable. This triggers a change in direction of the swirling rotations through which high levels of bending energy are discharged back into torsional form; see Fig. 5(d). The discharge of bending energy back into the torsional form also contributes to a small jump in the kinetic energy that passes through zero during the moment of reversal. Flipping thus involves the relaxation (or drop) of both bending and total strain energy.

Figure 5(b) illustrates that work done by the follower force, W_F, has almost the same rate of change and magnitude as the energy dissipated in the fluid medium, $W_{\mathbf{f}_M}$. This suggests that a much smaller proportion of the work done by active forces is stored in the system as strain energy. However, the constrained configuration allows for a periodic transfer of entire elastic energy in the torsional mode into and from bending, thus resulting in a dynamical trajectory with two distinct timescales of swirling and flipping.

F. Frequencies of oscillations: Swirling and flipping frequencies

This section examines the sensitivity of steady state oscillations to both prestress and force intensity. Figure 6, top row, shows the rates of both swirling and flipping dynamics as a function of follower force intensity and prestress. The results belong to three distinct prestress values,

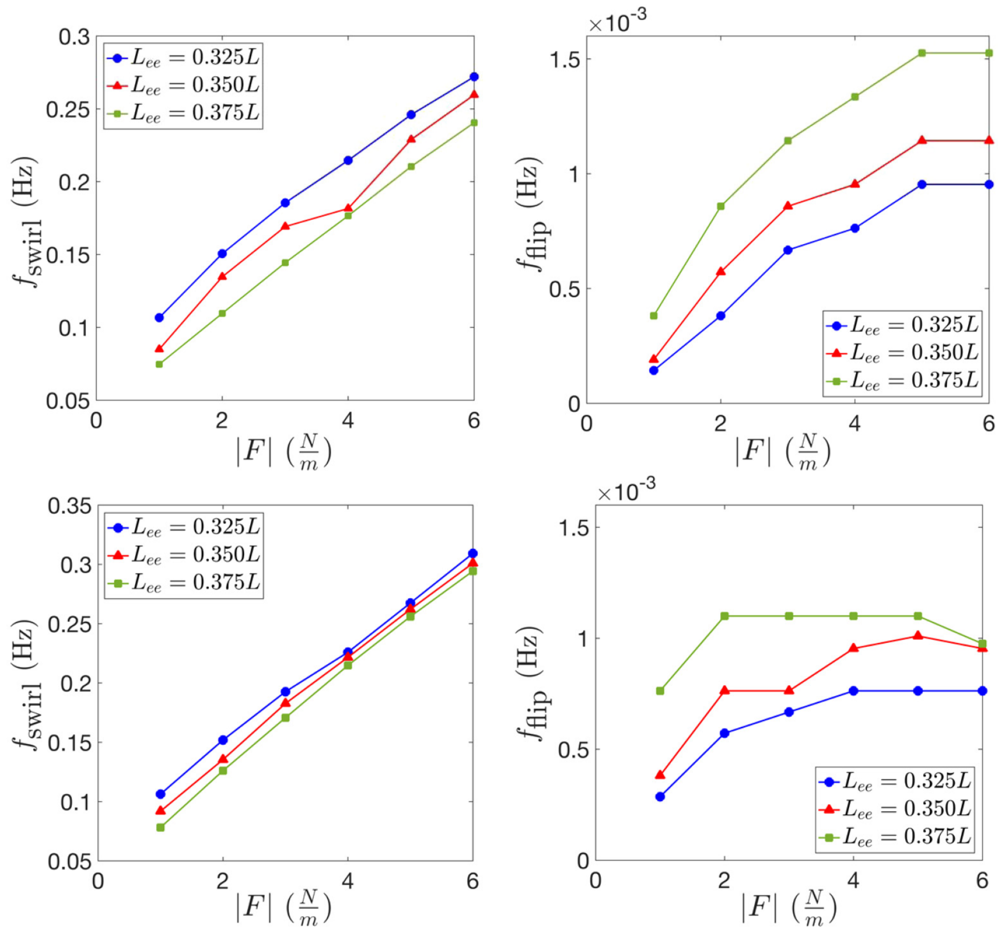

FIG. 6. The swirling frequency and the rate of flipping as a function of follower force density in the interval $0.325 \leqslant L_{ee}/L \leqslant 0.375$ and for $A = 0.8$ are shown in panels (a) and (b), respectively. The results reveal that for a fixed value of follower force by enhancing the end-to-end compression (reducing L_{ee}) the swirling frequency, f_{swirl}, increases, while the rate of flipping, f_{flip}, decreases. We also find that f_{swirl} increases roughly linearly with the follower force intensity (over the range investigated), but f_{flip} initially increases and then becomes insensitive to the force intensity. The results for a rod with the same A value but with bending and torsional stiffness B and T half of those given in Table I are also shown in panels (c) and (d). For this softer filament we find frequency of rotations to be more sensitive to the follower force and less sensitive to the compression L_{ee}.

$L_{ee}/L = \{0.325, 0.350, 0.375\}$. In all cases, we find that swirling frequency, f_{swirl}, linearly varies with follower force intensity, while having a low sensitivity to the prestress. On the other hand, the flipping frequency, f_{flip}, shown in the same figure is found to be more sensitive to the prestress values and becomes approximately independent of the follower force for very large active force densities.

We find that the rate of flipping seems to saturate to a value that depends on the initial compression ratio L_{ee}/L. More generally, our computations suggest that swirling rates seem very sensitive to the follower force and drag while flipping rates are dominantly determined by the interplay of bending and torsion. Keeping F constant while varying the initial level of prestress results in an increase in the swirling rate but a decrease in the flipping rate.

G. Role of elasticity parameters *B* and *T*

To understand the effect of elasticity, which is captured in our model with parameters B and T representing bending and torsional stiffness, respectively, we keep all other properties constant and examine the dynamics of a filament with bending and torsional stiffness twice as small as the values reported in Table I. Figures 6(c) and 6(d) show the results for prestress rates belonging to $L_{ee}/L = \{0.325, 0.350, 0.375\}$. For the softer filament with smaller elastic properties we find the relationship between the rotational frequency and the follower force to be linear although with a larger slope compared to the stiffer rod shown in Figs. 6(a) and 6(b). This can be explained by the fact that rotational oscillations in this regime emerge by the interplay of (1) active energy entering the system, (2) elastic energy of bending and torsion, and (3) energy dissipated due to fluid viscosity. During rotational cycles in between flapping events, part of the active energy must be spent on increasing the strain energy of the system [see green curve, E_s, in Fig. 5(a) (i)]. For the softer filament this strain energy barrier is smaller; hence a larger portion of active energy remains available to overcome fluid resistance and to gain rotational momentum. The rate of swirling, f_{swirl}, is calculated by taking the Fourier transformation of the bending curvature about one of the filament's two axes of bending, namely κ_1, over at least four cycles of flipping at $s = L/2$. The flipping

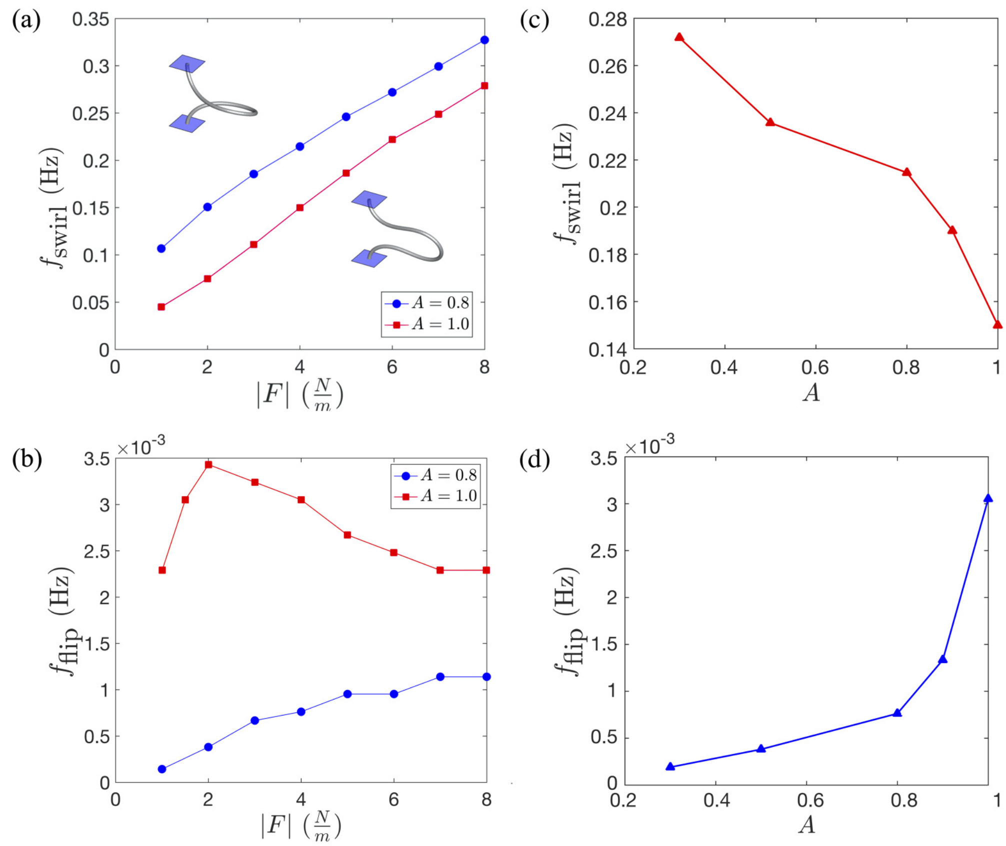

FIG. 7. Frequency of oscillations as a function of follower force density is compared for torsional-to-bending stiffness ratios varying from $A = 0.8$ to $A = 1.0$ (by keeping the bending stiffness constant at the value given in Table I, and increasing the torsional stiffness, T), and for prestress level of $L_{\mathrm{ee}}/L = 0.325$. Panel (a) shows that by increasing A (with F fixed), the torsional deflection of the base states decreases and so do the swirling frequencies f_{swirl}. In contrast, we find that for fixed F, the frequency of flips is higher for the larger value of A (1.0 compared to 0.8). Note also the intriguing result that for $A = 0.8$, the flipping rate increases with F. At the higher value of $A = 1$, however, we observe a nonmonotonic regime with an increase followed by a steady decrease in f_{flip} with F. Panels (c) and (d) show the dependency of swirling and flipping frequencies on the variations of A when the slack and force intensity are kept constant ($F = 4$ N/m, $L_{\mathrm{ee}}/L = 0.325$). By increasing A the torsional deflection decreases which results in a smaller swirling frequency. However, by increasing A the internal stresses decrease (as shown in Fig. 1) which results in larger flipping frequency.

frequency, f_{flip}, on the other hand is found via the Fourier transformation of torsion, κ_3, over the same time interval at the same cross section.

For the flipping frequency we find a response pattern similar to the filament with larger stiffness; however the saturation frequencies, i.e., the rate at which flipping rates become independent of the follower force, are smaller for softer filaments. Moreover, for the softer filament we observe a diminished sensitivity of both swirling and flipping rates to the prestress in comparison to the stiffer rod. This is due to the fact that for the softer filament, restoring effects at the base states (e.g., $P_{\mathrm{cr}}^{FF} = 4\pi^2 B/L^2$) are relatively smaller too.

We then examine the role of torsional-to-bending stiffness ratio, A, on swirling and flapping. For that, we keep the bending stiffness, B, constant (at the value given in Table I) and increase the torsional stiffness, T, to enlarge A from 0.8 to 1.0. As shown in Fig. 7, the base state with $A = 1.0$ has much smaller torsional deflection compared to the rod with $A = 0.8$ for the same compression level of $L_{\mathrm{ee}}/L = 0.325$. When a follower force is applied to these two base states we find that larger torsional-to-bending stiffness ratio results in smaller swirling frequencies, which nonetheless vary with a similar slope against force density.

The rod with larger A exhibits smaller out-of-plane deflection, when all else is kept constant, and thus the follower forces generate smaller net moments that in turn give rise to smaller swirling frequencies, compared to the application of the same forces to the rod with smaller A and larger out-of-plane deflection.

While the difference in the functional dependence of f_{flip} on F for $A = 0.8$ and $A = 1.0$ may be surprising, a possible explanation can be recognized by considering more closely the value of $L_{\mathrm{ee}}/L = 0.325$ and the distance the base state is located from the secondary bifurcation point. The inset is a close-up of Fig. 1(a) (iv). Since $1 - L_{\mathrm{ee}}/L = 0.625$ which for $A = 1.0$ is closer to the secondary bifurcation point than $A = 0.8$, this suggests that the absolute values of L_{ee}/L and the value of A control the frequencies. The shape of the base state and the energies stored in this state are thus very different.

Synthesizing our observations together, we find that the swirl-flip combination—the periodic changes in direction of the swirling rotations—is intricately associated with a specific sequence of energy interchanges between bending and torsional deformation modes of the filament. The nonconservative and configuration slaved dependence of the follower force direction succeed in mediating this transfer even as the magnitude of the follower force is fixed. In this respect, our system may also be considered as generating relaxation oscillations due to the effect of periodic excitation forces, except that here the frequency of this excitation is not imposed but emergent.

We deduce that the swirl-flip-swirl sequence is a self-generated emergent oscillation controlled intrinsically by the fact that an initially planar filament is unbiased insofar as the direction of swirling is concerned by the fact that the clamped-clamped filament is torsionally constrained. Indeed, relaxing the constraint at one end by converting the boundary conditions to a clamped-free cantilever type and approximating distributed follower forces by a single follower force exerted at the free tip (see Fig. 8 and, in the Supplemental Material [73], ESM Movie 6) results in the loss of the flips and continuous swirling.

H. Linear and nonlinear drag forms yield qualitatively similar spatiotemporal dynamics and oscillations

In this section we summarize a subset of computations performed using the linear resistivity drag (valid for Stokes flow) as described by Eq. (8) for the fluid force per unit length on the rod rather than the quadratic Morison form given by Eq. (7). Our goal is to ascertain whether the change from quadratic to linear drag changes the qualitative picture we have just described and analyzed in detail—specifically, the emergence of swirling oscillations characterized by a long timescale interspersed with very sharp flips that change the direction of the rotational motion.

Figure 9 illustrates the results both for the variations of swirling and flipping frequencies against the force intensity [panels (a) and (b)] and the emergence of limit-cycle instabilities [panels (c) and (d)]. Comparing Fig. 9(c) with Fig. 8(c) demonstrates that changing the form of the drag coefficient does not qualitatively change the type of solutions and bifurcations observed. Quantitatively, we find that swirling frequencies are changed as the dissipation due to activity changes. Over the narrow range of $|F|$ values plotted in Fig. 9(a), it is seen that the frequency increases with the magnitude of the follower force density. Note however that for very large values of $|F|$, we *do not* expect to see a linear increase. Rather, as in the case of Morison drag, dissipation due to viscous drag needs to balance active work done by the follower force; this requires that the swirling frequency vary with a power law different from that for the Morison case.

IV. PERSPECTIVES: CONNECTIONS TO RELAXATION OSCILLATIONS

The results presented in Sec. III for the clamped-clamped filament combined with results for the continuous swirling of an cantilevered active rod [Fig. 8(a), with no torsional constraints at $s = 0$] suggest that flipping involves the relaxation (or periodic and slow variations) of both bending and total strain energy. The discharge of bending energy back into the torsional form also contributes to a small jump in the kinetic energy that passes through zero during the moment of reversal. The role of filament inertia—as included in the time derivative terms in Eqs. (1) and (2)—in perhaps enabling overshoot and thus a change in the sign of the rotation direction is unclear and requires future exploration.

In the absence of active forces, fluid drag competes with physical mechanisms that temporarily store energy and produced damped motions. One of us has previously worked on theoretical and experimental systems with solid-fluid interactions where bulk solid elasticity provides the storage mechanism [54], as well as in purely fluid-fluid contexts with surface tension serving to store energy temporarily [76,77]. Here in the active context, fluid drag plays a crucial dual role: both dissipating the energy and providing a pathway to stabilize the system by forcing the emergence of oscillations with large amplitude and clear frequencies. The dependence of the frequencies on the active force density F follows power laws as shown in previous theoretical work by us [54,66]); the exact exponent depends (provided one is far from onset) on the form of the drag and is $5/6$ for quadratic drag as shown here, and $4/3$ for linear drag forms such as low Reynolds number Stokes drag.

We can make further connections to the classical relaxation oscillations eponymous with van der Pol's paper [67] studied in relation to self-sustaining nonlinear oscillations in triode circuits. Self-oscillating relaxation oscillations have been observed in electromagnetic devices [78], semiconductor laser devices subject to feedback concomitantly with optical injection [79], in the context of acoustics and music [80], and more recently found ubiquitously in cell and system biology contexts (see [81,82] and references therein). In many of these instances, coupled positive and negative feedback loops are hypothesized to yield hysteretic relaxation oscillations. An alternate hypothesis suggests that the essential ingredients of relaxation oscillators are a threshold device that enables a switch in direction, for example a bistable system, and a negative feedback loop. These ingredients are for instance the main components of the van der Pol oscillator in systems dynamics, and the Fitzhugh-Nagumo oscillator [83], Morris-Lecar [84] oscillators studied in neurobiology, and the comparator based extension of the Pearson-Anson oscillator [85]. In the system we studied extensively and presented in this article analogs to each component exist with the active follower force serving as the source of power.

We propose that the stable long-time relaxation oscillations in our system can be modeled in a simpler manner by studying the swirl-lip phenomenon as a two-timescale problem—with one time constant being much larger than the other. The challenge here would be to identify the minimal set of variables and parameters and is the subject of current work. Nonetheless, Eqs. (1)–(7) together constitute a complex but complete set of time-stepper equations that in conjunction with continuation and bifurcation techniques may be used to analyze the stability of time-dependent states as well as identify the critical points of onset.

V. SUMMARY

In this paper we have used a geometrically nonlinear continuum rod model to analyze the stable two- and three-

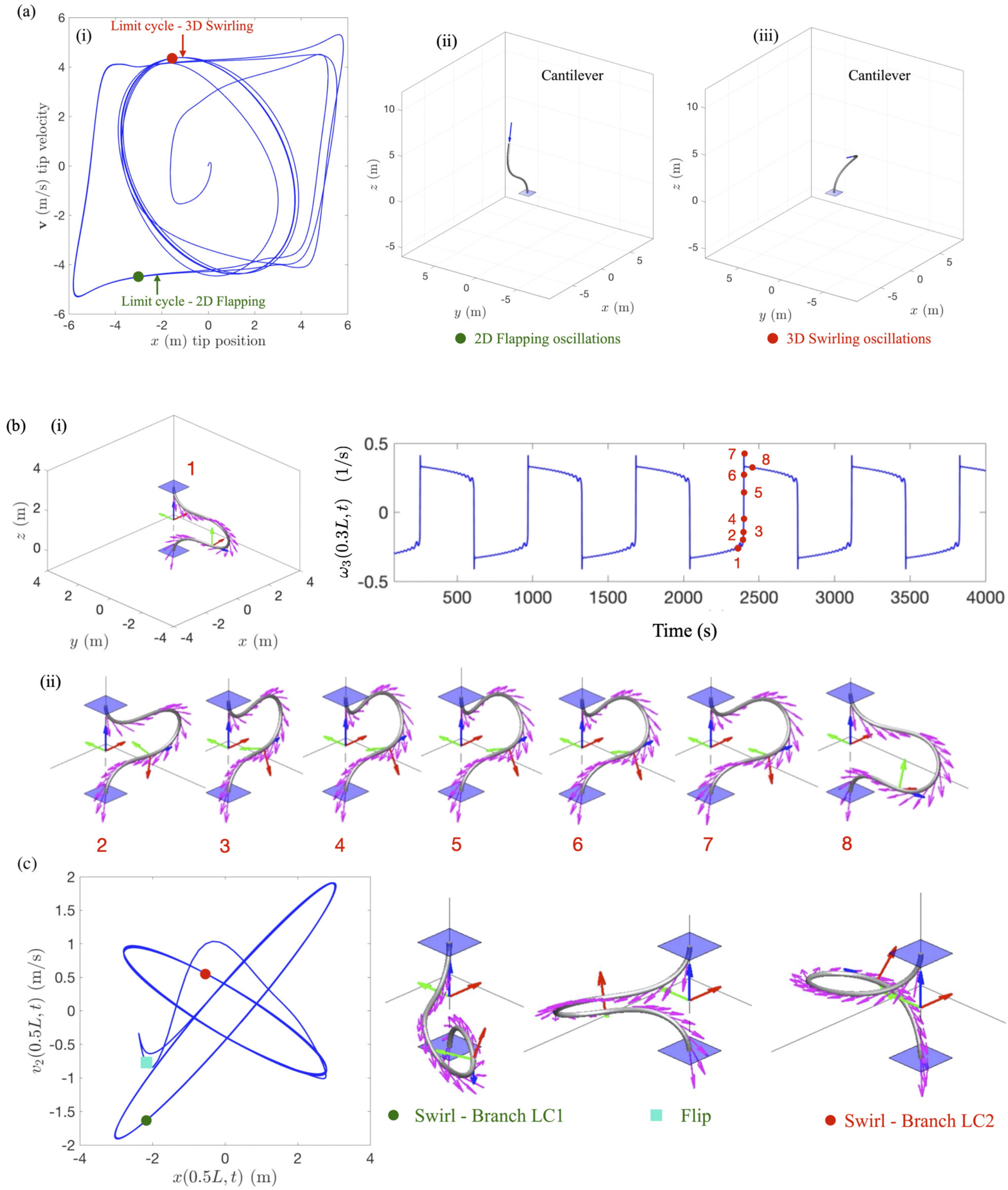

FIG. 8. Limit cycles for oscillatory instabilities: (a) active cantilever rods, and (b), (c) fixed-fixed prestressed rods. (a) Results for a partially constrained cantilevered rod with no prestress subject to follower force (see also ESM Movie 6 in the Supplemental Material [73]) when $f_3(L) = -20.2\pi^2 B/4L^2$. (i) and (ii) We show the limit cycle and a typical shape for flapping modes (green). The limit cycle in (i) features the velocity of the free end of the tip as a function of its vertical height. (ii) Here, only planar disturbances are imposed. (iii) When three-dimensional disturbances are allowed rod oscillations are fully three-dimensional with continuous swirling; see limit cycle in (i) and snapshot in (iii). (b) Here we show the sequence of shapes (time instants 1 to 8; see ESM Movie 5 in the Supplemental Material [73]) for the swirl-flip transitions. The parameters are $F = 4$, $L_{ee}/L = 0.4$, and $A = 0.8$. Note the overshoot seen between numbers 6 and 8. (c) Illustration of the swirl-flip limit cycles for the same parameters as in (b). We show only a few cycles immediately before (when the dynamics corresponds to branch LC1) and after the swirl (when the dynamics correspond to branch LC2). The limit cycles are not absolutely coincident due to the gradual changes in energy described in Sec. III E.

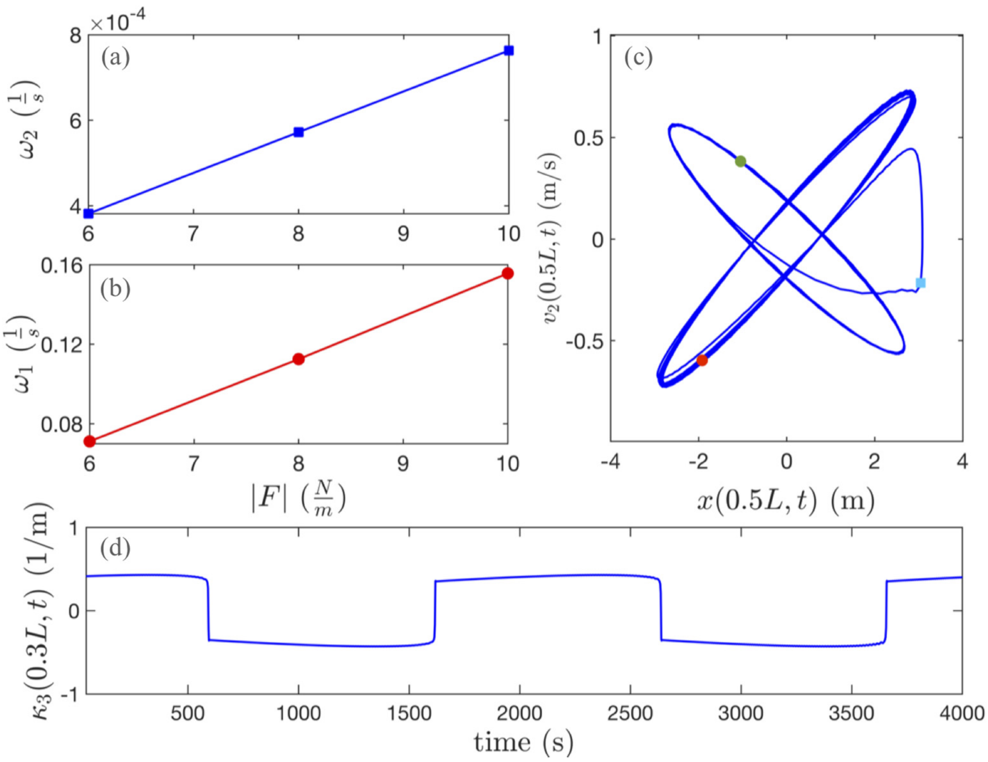

FIG. 9. Limit cycles for oscillatory instabilities when the fluid drag is computed using the expression for Stokes drag: (a) and (b) exhibit the rate of flipping and swirling oscillations, respectively, while (c) and (d) illustrate the swirl-flip limit cycles. The parameters used are $F = 8$, $L_{ee}/L = 0.375$, and $A = 0.8$.

dimensional oscillations of strongly constrained prestressed rods activated by distributed follower forces. A dissipative component resisting rod motion was imposed by assuming that the ambient fluid medium exerts a resisting quadratic drag following Morison's form corresponding to flow fields characterized by $O(1)$ and higher Reynolds numbers. Nonetheless, based on our previous work on planar flapping with both linear and nonlinear drag models, we expect our results to change quantitatively but not qualitatively for a different drag force such as the linear drag valid at low Reynolds number.

Our results from this work can be summarized as follows. For rods buckled to bent and twisted base states, we observe a swirling motion around the end-to-end axis under any nonzero follower force. Moreover, a second characteristic timescale of this motion is identified by the rate in which swirling motion undergoes reversal of direction, or flipping. We analyzed the force-frequency behavior as a function of prestress, measured by end-to-end compression, as well as material elasticity. For the range of parameters examined here we identify a linear relationship between the force density and swirling frequencies. The flipping rate is found to be sensitive to the force density only when forces are small. When force intensity increases flapping becomes independent of the force and is only a function of compression and torsional deflection.

To conclude, the dynamical responses of passive (See Fig. 10) and animated (see Figs. 6–11) prestressed rods constitute a rich, involved tapestry. Tuning the prestress and rod elasticity allows us to choose stable solutions from possible planar (2D) and twisted (3D) oscillating states. The connection to relaxation oscillations motivates future theoretical work that will help uncover the mechanistic and dynamical principles, and allow for phenomenological physical extensions of the theory to understand the role of inertia and other forms of fluid drag on the eventual spatiotemporal patterns attained. Practically, our results suggest avenues by which prestress, elasticity, and activity may be used to as knobs in exploiting active elasto-hydrodynamic instabilities to design synthetic macroscale fluidic elements such as pumps or mixers; see for instance Ref. [86].

APPENDIX A: DRAG COEFFICIENTS IN THE HIGH REYNOLDS NUMBER LIMIT

The Morison formula is a phenomenological formula that provides the net force on a long cylindrical body at moderate to high Reynolds numbers. The total force is here decomposed into a drag force per unit length that depends on the velocity and an inertial force per unit length that depends on the acceleration as given below:

$$\mathbf{f}_M = \frac{1}{2}\rho d C_d |\mathbf{v}|\mathbf{v} + \frac{1}{4}\pi \rho d^2 C_m \frac{d\mathbf{v}}{dt}. \tag{A1}$$

In this equation, ρ is the density of ambient fluid, d is the diameter of the cylindrical rod, $\mathbf{v}$ the speed of the cylinder with respect to the ambient, and t is time. The drag coefficient, C_d, and the inertia coefficient, C_m, are evaluated using experimental measurements and are sensitive to the characteristics of the flow such as Reynolds number as well as the properties of the cylindrical rod such as surface roughness and slenderness ratio. Edge effects due to the finite length of the cylindrical rod

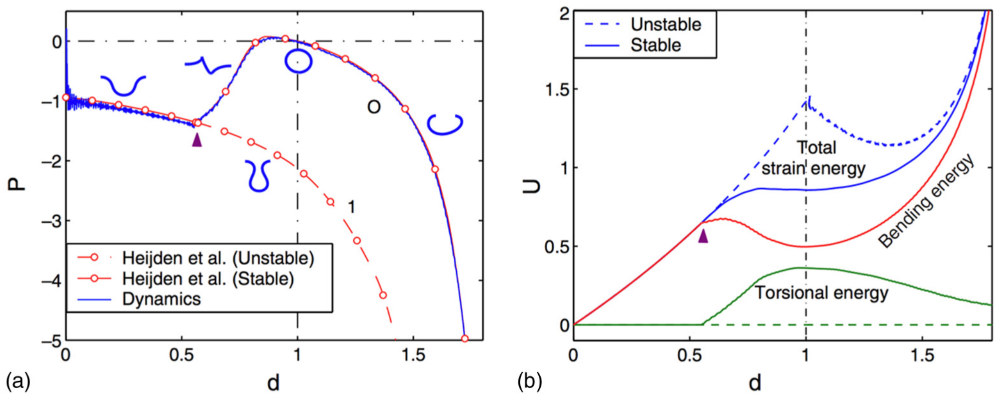

FIG. 10. (a) The tension force at the boundary, P, and (b) the strain energy, U, are plotted as functions of the end-to-end distance. As the out-of-plane bifurcation occurs, the bending energy decreases and torsional energy increases while the combined effect is a reduction in the total strain energy of the rod which favor the out-of-plane bifurcation.

are neglected. We choose to use (1) to also represent the drag in the case of a moving flexible active slender rod analyzed in this paper for reasons descried below; note also that the length L is much larger than the diameter ($L \gg d$) so that edge effects are small. The reduction sought is to encapsulate the effect of the fluid on the moving deforming rod in terms of an effective drag per unit length that serves as a lower-dimensional description of the fluid-solid interaction. Once this reduction is employed, the actual flow fields in the fluid are ignored.

Consider a deformed slender cable or filament as described earlier that is swirling slowly (rotational motion) in a fluid quiescent far from the cable. There are two ways by which time-periodic fluid flow fields may be generated.

First, when cross sections of the rod are executing rotations about the line joining the ends of the rod (swirling motion), oscillatory flow fields can be set up in the fluid with a timescale comparable to the time for a single rotation. For instance the center point when laterally displaced by a distance R and moving with angular velocity Ω (and thus moving through the fluid with relative speed ΩR) will generate ambient rotational flows with length scales R and timescales Ω^{-1}. We note that while the deformed rod is executing periodic motion, cross sections of the cylinder do not oscillate about the centerline. The rod here samples transient time periodic flows as it swirls through the fluid.

Second, slender cylinders moving through a fluid at moderate to large Reynolds number shed vortices; this process is associated with a shedding frequency characterized by the Strouhal number. In our case when the rotation is slow, the representative center point on the cylinder as it moves may shed vortices at a frequency $\Omega' \neq \Omega$ and instead set by its translational speed ΩR.

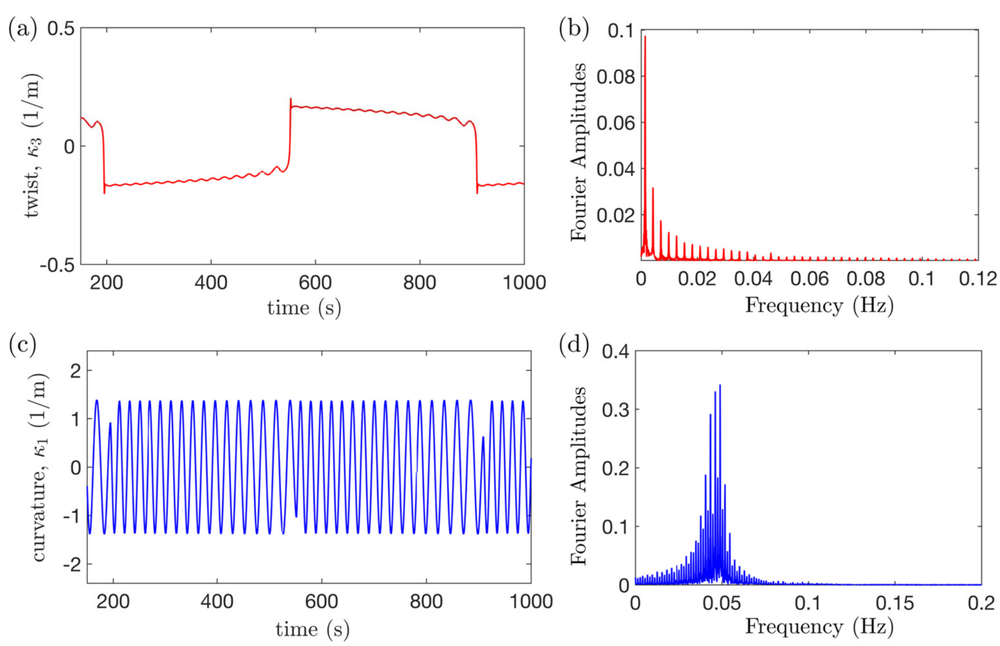

FIG. 11. Swirling and flipping frequencies are calculated by taking the Fourier transform of the curvature and twist at the midspan of the rod. The top row [(a), (b)] shows the twist data and the bottom row curvature [(c), (d)] for $A = 0.8$, $F = 1$ N, and $L_{ee}/L = 0.4$. The peaks in the frequency domain represent the dominant frequency of each plot.

The unsteady flows in the two scenarios described above can be quantified by the associated Keulegan-Carpenter number $K \equiv |\mathbf{v}|T/d$ with T being a suitable timescale. Thus the two sources of unsteadiness map to dimensionless numbers $K_1 = R/d$ and $K_2 = K_1(\Omega/\Omega')$. In reality, the above picture is simplified since in deformed rods each material point moves with a different value of R. Very importantly, in the case of the actively driven rod, the slow rotational frequency of the rod and any associated local vortex shedding frequencies cannot be determined *a priori* as these are emergent solutions. That is, the forms for the drag coefficients are unknown and cannot be determined before solving the problem. Nonetheless to obtain a reduced-dimensional form of the drag felt by the moving deformed rod, that reasonably captures the physics, we proceed as follows.

First, we look to previous studies on drag coefficients. It is established [71,72,87] that for large values of $\beta = d^2/\nu T$ (ν being the kinematic viscosity of the ambient fluid) the simple approximations hold:

$$C_d = \frac{3\pi^3}{2K}\left[(\pi\beta)^{-\frac{1}{2}} + (\pi\beta)^{-1}\right], \tag{A2}$$

$$C_m = 2 + 4(\pi\beta)^{-\frac{1}{2}}. \tag{A3}$$

Our emergent rotational frequencies, associated deformations, and ambient fluid properties correspond to moderate values of β ($\beta < 70$) and hence (2) and (3) are not quite appropriate. Furthermore the K values associated with our simulations based on the emergent solutions are much higher (a representative value being $K \approx 800$) than those for which (2) and (3) have been tested. For instance Fig. 1 of [87] and [71,72] correspond to K values that fall in much smaller range $K < 20$.

Since there are no empirical data available for the rod properties chosen in our study, and since the drag coefficient cannot be calculated *a priori*, we use the previous results that compare (2) and (3) with experimental data from the referenced papers to estimate approximate drag coefficients. We note that the average value of $C_d \approx 1$ usually pertains to rods with the slenderness ratio that is one order of magnitude smaller (e.g., 10 or 25 as in [72]) than the ratio used in our simulations. We have chosen the slenderness ratio of the rod to be 800 (motivated by literature [29]). Figures 1–4 of [87] then suggest that for $K \approx 800$ the drag coefficient is expected to be an order of magnitude smaller than 1 (by a factor of 40). Since the K value based on vortex shedding is estimated to be between 800 and around 50, we chose a drag coefficient value equal to 0.1 that is between 1 and 1/40. This is also consistent with forms previously used for deforming cables or rods with similar slender geometries [64].

In our study the range of frequencies pertaining to swirling and flipping lie between 0.1–0.35 Hz. In this interval the drag component of the Morison formula is more important (always larger) than the inertial component. Given that our aim is to understand the spatiotemporal dynamics generated by the interplay between elasticity and the nonconservative follower force, we would like the dissipative component (i.e., the drag) to represent simple yet physically meaningful forms. Thus we choose the quadratic term associated with C_d for the nonlinear regime and ignore the inertial contribution.

Note that we have also analyzed the dynamics for linear drag proportional to v as happens for the Stokes low Reynolds number regime. The details of the latter are in the main narrative and are not included here.

APPENDIX B: EFFECT OF ADDED MASS

Added mass takes into account the inertial force required for an object to accelerate in a fluid, in addition to the inertial force of the body's own mass. For an object with cylindrical shape added mass is $m_a = V\rho_f$ with V representing the volume of the cylinder. Therefore in our model the effect of added mass can be captured by adding the density of water to the density of the solid material in the equations of motion. In other words, we can consider our current results in the paper to belong to a rod with density $\rho_{s2} = \rho_{s1} - \rho_f$ where ρ_{s1} is the density of the rod reported in Table I of the main narrative.

APPENDIX C: CALCULATING FREQUENCIES BY FOURIER TRANSFORM

Figure 11 shows the curvature and twist in both time and frequency domains. We calculate the frequency of oscillations using the Fourier transform of the curvature and twist at $s = L/2$. The rate of swirling, $f_{\rm swirl}$, is calculated by taking the Fourier transform of the bending curvature about one of the filaments's two axes of bending, namely κ_1, over at least four cycles of flipping. The flipping frequency, $f_{\rm flip}$, on the other hand is found via the Fourier transformation of the twist, κ_3, over the same time interval that is used for the calculation of the swirling frequency. Using the results shown in panels (b) and (d) of Fig. 11, the maximum values of Fourier amplitudes are selected as the frequency in each case.

[1] W. A. Oldfather, C. A. Ellis, and D. M. Brown, Leonhard Euler's elastic curves, Isis **20**, 72 (1933).

[2] I. Todhunter and K. Pearson, *A History of the Theory of Elasticity and of the Strength of Materials: From Galilei to the Present Time, Vol. 2, Part 1, Saint-Venant to Lord Kelvin* (Dover Publications United States, 1893).

[3] S. Timoshenko, *History of Strength of Materials: With a Brief Account of the History of Theory of Elasticity and Theory of Structures*, Dover Civil and Mechanical Engineering Series (Dover Publications, Italy, 1983).

[4] L. Euler and C. Truesdell, *The Rational Mechanics of Flexible or Elastic Bodies 1638–1788*, Introduction to Vols. X and XI, Leonhard Euler, Opera Omnia (Springer-Verlag, Germany, 1960).

[5] S. Timoshenko and J. Gere, *Theory of Elastic Stability*, Dover Civil and Mechanical Engineering Series (Dover Publications, New York, 2009).

[6] M. Nizette and A. Goriely, Towards a classification of Euler-Kirchhoff filaments, J. Math. Phys. **40**, 2830 (1999).

[7] Theory of rods deforming in space, in *Nonlinear Problems of Elasticity* (Springer, New York, 2005), pp. 269–344.

[8] G. W. Hunt, G. J. Lord, and M. A. Peletier, Cylindrical shell buckling: A characterization of localization and periodicity, Discrete and Continuous Dynamical Systems B **3**, 505 (2003).

[9] R. Ogden, *Non-linear Elastic Deformations*, Dover Civil and Mechanical Engineering Series (Dover Publications, United States, 1997).

[10] M. A. Biot, *Mechanics of Incremental Deformations* (Wiley, New York , 1965).

[11] F. Gittes, B. Mickey, J. Nettleton, and J. Howard, Flexural rigidity of microtubules and actin filaments measured from thermal fluctuations in shape, J. Cell Biol. **120**, 923 (1993).

[12] C. A. Weber, R. Suzuki, V. Schaller, I. S. Aranson, A. R. Bausch, and E. Frey, Random bursts determine dynamics of active filaments, Proc. Natl. Acad. Sci. USA **112**, 10703 (2015).

[13] A. Gopinath and L. Mahadevan, Elastohydrodynamics of wet bristles, carpets and brushes, Proc. R. Soc. A **467**, 1665 (2011).

[14] K. Niklas, *Plant Biomechanics: An Engineering Approach to Plant Form and Function* (University of Chicago Press, United Kingdom, 1992).

[15] J. Howard, Molecular mechanics of cells and tissues, Cell. Mol. Bioeng. **1**, 24 (2008).

[16] F. Gibbons, J. F. Chauwin, M. Despósito, and J. V. José, A dynamical model of kinesin-microtubule motility assays, Biophys. J. **80**, 2515 (2001).

[17] J. Howard, A. J. Hudspeth, and R. D. Vale, Movement of microtubules by single kinesin molecules, Nature (London) **342**, 154 (1989).

[18] A. Vaziri and A. Gopinath, Cell and biomolecular mechanics in silico, Nat. Mater. **7**, 15 (2008).

[19] C. Ainsworth, Tails of the unexpected, Nature (London) **448**, 638 (2007).

[20] P. V. Bayly and S. K. Dutcher, Steady dynein forces induce flutter instability and propagating waves in mathematical models of flagella, J. R. Soc., Interface **13**, 20160523 (2016).

[21] P. Bayly and K. Wilson, Equations of interdoublet separation during flagella motion reveal mechanisms of wave propagation and instability, Biophys. J. **107**, 1756 (2014).

[22] P. Robison, M. A. Caporizzo, H. Ahmadzadeh, A. I. Bogush, C. Y. Chen, K. B. Margulies, V. B. Shenoy, and B. L. Prosser, Detyrosinated microtubules buckle and bear load in contracting cardiomyocytes, Science **352**, aaf0659 (2016).

[23] J. B. Keller, The shape of the strongest column, Arch. Ration. Mech. Anal. **5**, 275 (1960).

[24] J. B. Keller and F. I. Niordson, The tallest column, J. Math. Mech. **16**, 433 (1966).

[25] I. Elishakoff, Controversy associated with the so-called "follower forces": Critical overview, Appl. Mech. Rev. **58**, 117 (2005).

[26] K. A. McHugh and E. H. Dowell, Nonlinear response of an inextensible, cantilevered beam subjected to a nonconservative follower force, ASME. J. Comput. Nonlinear Dyn. **14**, 031004 (2019).

[27] L. Pigolotti, C. Mannini, G. Bartoli, and K. Thiele, Critical and post-critical behavior of two-degree-of-freedom flutter-based generators, J. Sound Vib. **404**, 116 (2017).

[28] C. Brennen and H. Winet, Fluid mechanics of propulsion by cilia and flagella, Annu. Rev. Fluid Mech. **9**, 339 (1977).

[29] F. Ling, H. Guo, and E. Kanso, Instability-driven oscillations of elastic microfilaments, J. R. Soc., Interface **15**, 20180594 (2018).

[30] Y. L. Zhang and D. M. Crothers, Statistical mechanics of sequence-dependent circular DNA and its application for DNA cyclization, Biophys. J. **84**, 136 (2003).

[31] P. Satir and T. Matsuoka, Splitting the ciliary axoneme: Implications for a "switch-point" model of dynein arm activity in ciliary motion, Cell Motil. **14**, 345 (1989).

[32] C. J. Brokaw, Thinking about flagellar oscillation, Cell Motil. **66**, 425 (2009).

[33] D. M. Woolley, Flagellar oscillation: A commentary on proposed mechanisms, Biol. Rev. **85**, 453 (2010).

[34] I. H. Riedel-Kruse, A. Hilfinger, J. Howard, and F. Jülicher, How molecular motors shape the flagellar beat, HFSP J. **1**, 192 (2007).

[35] C. B. Lindemann and K. A. Lesich, Flagellar and ciliary beating: The proven and the possible, J. Cell Sci. **123**, 519 (2010).

[36] D. Bray, *Cell Movements: From Molecules to Motility* (Garland Science, New York, 2001).

[37] S. Nonaka, H. Shiratori, Y. Saijoh, and H. Hamada, Determination of left–right patterning of the mouse embryo by artificial nodal flow, Nature (London) **418**, 96 (2002).

[38] A. M. D. Malone, C. T. Anderson, P. Tummala, R. Y. Kwon, T. R. Johnston, T. Stearns, and C. R. Jacobs, Primary cilia mediate mechanosensing in bone cells by a calcium-independent mechanism, Proc. Natl. Acad. Sci. USA **104**, 13325 (2007).

[39] S. Hanasoge, P. J. Hesketh, and A. Alexeev, Microfluidic pumping using artificial magnetic cilia, Microsyst. Nanoeng. **4**, 11 (2018).

[40] R. Dreyfus, J. Baudry, M. L. Roper, M. Fermigier, H. A. Stone, and J. Bibette, Microscopic artificial swimmers, Nature (London) **437**, 862 (2005).

[41] D. Nishiguchi, J. Iwasawa, H.-R. Jiang, and M. Sano, Flagellar dynamics of chains of active janus particles fueled by an AC electric field, New J. Phys. **20**, 015002 (2018).

[42] A. E. Patteson, A. Gopinath, and P. E. Arratia, Active colloids in complex fluids, Curr. Opin. Colloid Interface Sci. **21**, 86 (2016).

[43] Y. Sasaki, Y. Takikawa, V. S. R. Jampani, H. Hoshikawa, T. Seto, C. Bahr, S. Herminghaus, Y. Hidaka, and H. Orihara, Colloidal caterpillars for cargo transportation., Soft Matter **10**, 8813 (2014).

[44] D. Bigoni, O. N. Kirillov, D. Misseroni, G. Noselli, and M. Tommasini, Flutter and divergence instability in the Pflüger column: Experimental evidence of the Ziegler destabilization paradox, J. Mech. Phys. Solids **116**, 99 (2018).

[45] H. H. E. Leipholz, *Stability of Elastic Systems* (Sijthoff and Noordhoff, Alphen aan den Rijn, the Netherlands, 1980), p. 474.

[46] G. M. L. Gladwell, Follower forces: Leipholz's early researches in elastic stability, Can. J. Civ. Eng. **17**, 277 (1990).

[47] V. V. Bolotin, *Nonconservative Problems of the Theory of Elastic Stability* (Macmillan, New York, 1963).

[48] A. Pfluger, *Stabilitatsprobleme der Elastostatik* (Springer-Verlag, Berlin, 1950), p. 217.

[49] H. Ziegler, Introduction, in *Principles of Structural Stability* (Birkhäuser Basel, Basel, 1977), pp. 1–43.

[50] W. G. Wood, S. S. Saw, and P. M. Saunders, The kinetic stability of a tangentially loaded strut, Proc. R. Soc. London A **313**, 239 (1969).

[51] V. V. Bolotin, Dynamic instabilities in mechanics of structures, Appl. Mech. Rev. **52**, R1 (1999).

[52] G. De Canio, E. Lauga, and R. E. Goldstein, Spontaneous oscillations of elastic filaments induced by molecular motors, J. R. Soc., Interface **14**, 20170491 (2017).

[53] R. Chelakkot, A. Gopinath, L. Mahadevan, and M. F. Hagan, Flagellar dynamics of a connected chain of active, polar, Brownian particles, J. R. Soc., Interface **11**, 20130884 (2014).

[54] Y. Fily, P. Subramanian, T. M. Schneider, R. Chelakkot, and A. Gopinath, Buckling instabilities and spatio-temporal dynamics of active elastic filaments, J. R. Soc., Interface **17**, 20190794 (2020).

[55] A. S. Sangani and A. Gopinath, Elastohydrodynamical instabilities of active filaments, arrays, and carpets analyzed using slender-body theory, Phys. Rev. Fluids **5**, 083101 (2020).

[56] H. J. Palanthandalam-Madapusi and S. Goyal, Robust estimation of nonlinear constitutive law from static equilibrium data for modeling the mechanics of DNA, Automatica **47**, 1175 (2011).

[57] S. Fatehiboroujeni, N. Petra, and S. Goyal, Linearized Bayesian inference for Young's modulus parameter field in an elastic model of slender structures, Proc. R. Soc. A **476**, 20190476 (2020).

[58] S. Liu, Z. Yao, K. Chiou, S. I. Stupp, and M. Olvera de la Cruz, Emergent perversions in the buckling of heterogeneous elastic strips, Proc. Natl. Acad. Sci. USA **113**, 7100 (2016).

[59] A. Goriely and M. Tabor, Spontaneous Helix Hand Reversal and Tendril Perversion in Climbing Plants, Phys. Rev. Lett. **80**, 1564 (1998).

[60] M. K. Jawed, F. Da, J. Joo, E. Grinspun, and P. M. Reis, Coiling of elastic rods on rigid substrates, Proc. Natl. Acad. Sci. USA **111**, 14663 (2014).

[61] A. Balaeff, L. Mahadevan, and K. Schulten, Modeling DNA loops using the theory of elasticity, Phys. Rev. E **73**, 031919 (2006).

[62] S. Goyal and N. Perkins, Looping mechanics of rods and DNA with non-homogeneous and discontinuous stiffness, Int. J. Non-Linear Mech. **43**, 1121 (2008).

[63] S. Forth, C. Deufel, M. Y. Sheinin, B. Daniels, J. Sethna, and M. D. Wang, Abrupt Buckling Transition Observed during the Plectoneme Formation of Individual DNA Molecules, Phys. Rev. Lett. **100**, 148301 (2008).

[64] S. Goyal, N. Perkins, and C. L. Lee, Non-linear dynamic intertwining of rods with self-contact, Int. J. Non-Linear Mech. **43**, 65 (2008).

[65] T. D. Lillian, M. Taranova, J. Wereszczynski, I. Andricioaei, and N. C. Perkins, A multiscale dynamic model of DNA supercoil relaxation by topoisomerase IB, Biophys. J. **100**, 2016 (2011).

[66] S. Fatehiboroujeni, A. Gopinath, and S. Goyal, Nonlinear oscillations induced by follower forces in prestressed clamped rods subjected to drag, J. Comput. Nonlinear Dyn. **13**, 121005 (2018).

[67] A. H. Nayfeh and D. T. Mook, Introduction, in *Nonlinear Oscillations* (John Wiley & Sons, United States, 2007), Chap. 1, pp. 1–38.

[68] G. Kirchhoff, Uber das gleichgewicht und die bewegung eines unendlich dunnen elastischen stabes, J. Reine Angew. Math. (Crelle) **56**, 285 (1859).

[69] S. Fatehiboroujeni, H. Palanthandalam-Madapusi, and S. Goyal, Computational rod model with user-defined nonlinear constitutive laws, J. Comput. Nonlinear Dyn. **13**, 101006 (2018).

[70] S. Goyal, N. C. Perkins, and C. L. Lee, Nonlinear dynamics and loop formation in Kirchhoff rods with implications to the mechanics of DNA and cables, J. Comput. Phys. **209**, 371 (2005).

[71] P. Fish, R. Dean, and N. Heaf, Fluid-structure interaction in Morison's equation for the design of offshore structures, Eng. Struct. **2**, 15 (1980).

[72] J. Wolfram and M. Naghipour, On the estimation of Morison force coefficients and their predictive accuracy for very rough circular cylinders, Appl. Ocean Res. **21**, 311 (1999).

[73] See Supplemental Material at http://link.aps.org/supplemental/10.1103/PhysRevE.103.013005 for a set of simulation results in video format.

[74] G. van der Heijden, S. Neukirch, V. Goss, and J. Thompson, Instability and self-contact phenomena in the writhing of clamped rods, Int. J. Mech. Sci. **45**, 161 (2003).

[75] S. Fatehiboroujeni, A. Gopinath, and S. Goyal, Effect of boundary constraints on the nonlinear flapping of filaments animated by follower forces, arXiv:1905.08421.

[76] A. Gopinath and D. L. Koch, Dynamics of droplet rebound from a weakly deformable gas-liquid interface, Phys. Fluids **13**, 3526 (2001).

[77] A. Gopinath and D. L. Koch, Collision and rebound of small droplets in an incompressible continuum gas, J. Fluid Mech. **454**, 145 (2002).

[78] D. Wang, Relaxation oscillators and networks, in *Wiley Encyclopedia of Electrical and Electronics Engineering* (John Wiley & Sons, Inc., New Jersey, 1999).

[79] M. Nizette and T. Erneux, Optical frequency dynamics and relaxation oscillations of a semiconductor laser subject to filtered optical feedback, in *Semiconductor Lasers and Laser Dynamics II*, Proc. SPIE, Vol. 6184, edited by D. Lenstra, M. Pessa, and I. H. White (SPIE, 2006), pp. 280–289.

[80] A. Jenkins, Self-oscillation, Phys. Rep. **525**, 167 (2013).

[81] M. B. Elowitz and S. Leibler, A synthetic oscillatory network of transcriptional regulators, Nature (London) **403**, 335 (2000).

[82] C. Kut, V. Golkhou, and J. S. Bader, Analytical approximations for the amplitude and period of a relaxation oscillator, BMC Systems Biology **3**, 6 (2009).

[83] R. Fitzhugh, Impulses and physiological states in theoretical models of nerve membrane, Biophys. J. **1**, 445 (1961).

[84] C. Morris and H. Lecar, Voltage oscillations in the barnacle giant muscle fiber, Biophys. J. **35**, 193 (1981).

[85] S. O. Pearson and H. S. G. Anson, The neon tube as a means of producing intermittent currents, Proc. Phys. Soc. London **34**, 204 (1921).

[86] R. Chelakkot, M. F. Hagan, and A. Gopinath, Synchronized oscillations, traveling waves, and jammed clusters induced by steric interactions in active filament arrays, Soft Matter, doi:10.1039/D0SM01162B (2021).

[87] T. Sarpkaya, Force on a circular cylinder in viscous oscillatory flow at low Keulegan-Carpenter numbers, J. Fluid Mech. **165**, 61 (1986).